# CONCEPTUAL DESIGN REPORT

# Scientific Instrument MID

January 2012, Web Version

*A. Madsen*

*for Scientific Instrument MID (WP83)*

*at the European XFEL*

# Contents

# Executive summary

The Materials Imaging and Dynamics (MID) instrument of the European XFEL facility will provide unique capabilities in materials imaging and dynamics experiments with particular focus on the application of coherent X-ray scattering and diffraction techniques. Coherent diffractive imaging (CDI) and X-ray photon correlation spectroscopy (XPCS) experiments are at the heart of the activities planned at the MID station, but also time-resolved scattering and imaging studies can be foreseen taking advantage of the time structure and high flux of the X-ray free-electron laser (XFEL) beam. In addition, the MID station will enable the use of high-energy photons, above 25 keV, in scattering and imaging experiments in materials science.

Scattering experiments will be performed in either wide- or small-angle scattering geometries with a 2D pixel detector featuring a spatial and temporal resolution compatible with the requirements, e.g. concerning speckle visibility and oversampling of the diffraction pattern as well as the time structure (4.5 MHz) of the XFEL. Adapted detectors are a major part of the MID baseline instrumentation and their importance should not be underestimated. It is very likely that one detector alone cannot meet all requirements. Other baseline instrumentation includes a general-purpose, in-vacuum SAXS/WAXS setup with the necessary degrees of freedom in sample motion and a very long horizontal detector arm. In addition, a heavy-duty, four-circle diffractometer with a vertical scattering option is part of the baseline instrumentation. A windowless beamline is preferred whenever possible. X-ray optics is necessary in the beam path to tailor the XFEL beam. For instance, to accommodate various types of experiments, the intensity incident on the sample, as well as the beam size and bandwidth ($\Delta E/E$), must be adjustable. Adequate beam diagnostics (e.g. timing, intensity) on the single shot level is necessary for many experiments. In other cases, lower frequency information (e.g. beam shape from YAG screens and position from quadrant diodes) is required. Together with optimized data acquisition and data transfer systems, as well as a computing infrastructure for rapid data reduction and analysis, it constitutes the backbone of the MID station.

The photon energy for coherent experiments of the MID instrument ranges from 5 to 25 keV, with possibilities also to cover 3–5 keV and > 25 keV by use of special optics. The MID station is located at the centre branch of the SASE2 beamline, necessitating only two horizontal offset mirrors in the beam path (to get around the major beam stop chicane). For this purpose, low-$Z$ covered mirrors can be employed up to ~ 20 keV. The use of metal-coated mirrors can extend this range up to more than 25 keV. For high-energy experiments, a double Laue crystal monochromator is required to monochromatize and transport the beam around the beam stop and reach the experiment hutch. Hence, the Laue DCM replaces the offset mirrors in this operation mode.

In the 5 to 25 keV range, both a pre-monochromator as well as high-resolution monochromators are required to reach the bandwidth of $10^{-5}$ that is necessary for some critical coherence experiments at the MID station. The monochromators must be appropriately cooled and placed as close as possible to the experiment to eliminate the effect of eventual angular fluctuations in the beam position on the sample. Being on the centre branch of SASE2, the MID station is logically placed towards the end on the experiment area, and hence a possible solution is to accommodate an optics hutch right upstream of the experiment hutch. This optics hutch will host the monochromators that will then be situated about 960 m from the source. The natural divergence of the XFEL beam will at this point result in a beam size of 1–3 mm (depending on the photon energy) that, together with appropriate cooling, will allow a large number of pulses from a train to pass the monochromator. The limiting factor is a heat bump on the crystal that will build up after only a few pulses if the effect of heat load is not minimized.

Focusing of the beam is possible by use of compound refractive lenses (CRL). A flexible, multi-CRL chamber (CRL transfocator) will be situated right after the monochromators to enable focusing at different energies. For experiments at a reduced repetition rate, or experiments not requiring a monochromator, it is foreseen to use a second CRL unit installed close to the source (~ 230 m) to make the beam parallel, or to focus at the sample position possibly using a refocusing scheme employing both the first and second CRL units.

For certain classes of experiments, it is desirable to modify the time structure of X-ray pulses within a train. For this purpose, X-ray split-delay lines, based on perfect crystals and grazing incidence mirrors, are installed. Due to challenges in efficient cooling while still maintaining the required positioning precision of the crystals, it is foreseen to always use a monochromator upstream of the crystal delay line.

The MID experimental hutch is located approximately 970 m downstream of the XFEL source in the SASE2 experiment area. The hutch needs to be about 8 m wide and 20 m long to accommodate local optics, sample environments, and the instrument with a 10 m long detector arm. This distance is required to be suitable for the proposed coherent scattering experiments, i.e. to overcome limitations of the 2D imaging detectors that presently are developed for the European XFEL. All detectors in this challenging R&D program have been specified to operate at 4.5 MHz (the pulse repetition rate within a train), but, currently, the pixel size is limited to > 200 $\mu$m; if smaller pixels were available, a correspondingly shorter sample-detector distance could be used without losses in signal-to-noise ratio.

The mission of the MID station is to be specialized in coherence applications while also covering a broad range of scattering and imaging experiments at the hard end of the energy spectrum. Not only does that require a maximum of flexibility in the beam parameters that can be delivered, but it also necessitates that different specialized sample environments can be integrated into the setup easily. The main equipment and optical components of the MID station are summarized in Table 1.

**Table 1:** *Summary of the MID characteristics*

| Parameter | Amount |
|---|---|
| Photon energy range | 5–25 keV (coherent) and > 25 keV<br>Option for 3–5 keV |
| Bunch charge | 1–1 000 pC |
| Polarization | Linear (horizontal) |
| Beamline optics | 2 offset mirrors, high-energy Laue mono, slit collimators, pre-mono, high-resolution mono, CRL transfocator units, split-delay lines, various local optics (close to the sample) |
| Monochromators | Pre-mono : Si(111) ($1.4 \times 10^{-4}$ BW)<br>High res. mono: Si(511) ($1.1 \times 10^{-5}$ BW)<br>Double Si or C* Laue monochromator (> 25 keV) |
| Pulse duration | 1–100 fs |
| Beam size on sample | 1–200 $\mu$m (by focusing and/or collimation) |
| Equipment | General-purpose SAXS/WAXS setup with very long horizontal detector arm<br>Four-circle diffractometer with vertical scattering capability<br>Single-pulse X-ray diagnostics<br>4.5 MHz 2D pixel detector (e.g. AGIPD)<br>2D pixel detector with high spatial resolution<br>4.5 MHz pump laser + diagnostics<br>DAQ and computer infrastructure |

# Introduction

When the European XFEL facility becomes operational in 2015, it will deliver the strongest X-ray beams ever produced. This means that X-ray scattering and imaging experiments can be taken into a new era. Together with the five other Phase I instruments,[1] the MID station is designed to fulfil this goal as outlined in the present conceptual design report (CDR). The high brilliance of the machine will, in particular, be important for cutting-edge experiments with coherent X-ray beams and in the study of fast and ultrafast dynamics. The MID instrument aims at giving the user community new opportunities to investigate the structure and dynamics of materials with unprecedented resolution in space and time. An important class of experiments concerns non-destructive measurements where the sample survives several SASE pulse and multiple exposures are hence possible taking advantage of the pulse train structure, as shown in Figure 1.
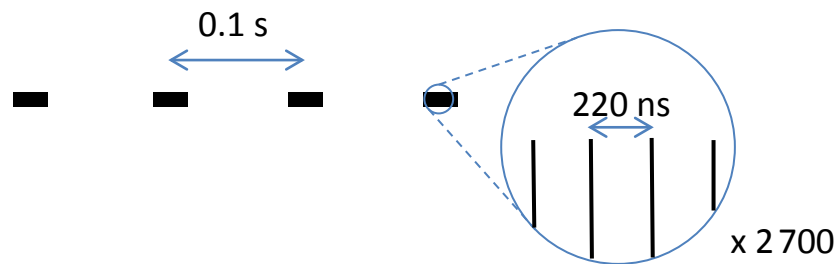


**Figure 1:** *Time structure of the European XFEL with 2 700 pulses at 4.5 MHz (within a pulse train) and an overall 10 Hz train repetition rate*

In 2015, the Linac Coherent Light Source (LCLS) at Stanford will have been operational for more than five years and, hence, at the European XFEL, it is natural to focus efforts on the outstanding properties with respect to LCLS. Here, the time structure of the machine with a higher average flux (27 000 pulses/s vs. 120 pulses/s at LCLS) first comes to mind. In particular, within a bunch train, the X-ray pulses are separated by only 220 ns, opening

---

[1] SPB & FXE (SASE1), MID & HED (SASE2), and SQS & SCS (SASE3)

up new possibilities in studies of fast dynamics and in high-throughput coherent scattering experiments. Capitalizing on the experience from synchrotron sources, the MID station is well placed to exploit this advantage and push CDI and XPCS to new frontiers.

However, to become successful, it is of outmost importance that investments in instrumentation are complemented by strong emphasis on enabling technologies, particularly concerning new detectors. The detector performance is of highest importance for the MID station and is the crucial factor of its data acquisition chain. Hence, this is a key point that is stressed in this CDR. With optimized and adapted detectors, there is no doubt that the MID station will take (time-resolved) structural determinations and dynamics studies in materials science far beyond the current capabilities at synchrotron sources. The scientific problems to be addressed comprise electronic, atomic, and molecular dynamics in liquids, glasses, and crystalline materials, as well as high-resolution structural investigations in materials-, nano-, and bio-physical sciences. The possibility to perform coherent scattering with a high flux up to 25 keV allows us, for the first time, to address problems in bulk materials science by XPCS and CDI.

The number of coherent photons expected per pulse at the XFEL is shown in Figure 2. Taking the partial coherence and natural bandwidth of synchrotron sources into account, the figure shows that the average coherent intensity (at $10^{-5}$ BW) is approximately a factor of $10^5$ larger than at ESRF or APS. This is a revolutionary high number and will inevitably lead to new scientific discoveries.
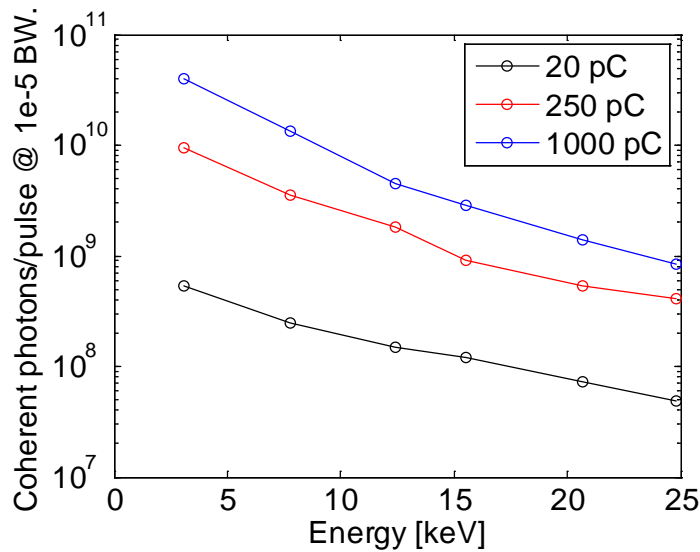
***Figure 2:*** *Number of coherent photons per pulse (one pulse every 220 ns inside a pulse train) expected at the European XFEL for different pulse charges and photon energies at $10^{-5}$ BW (figure based on calculations by Schneidmiller and Yurkov[2]). For example, an ordinate value of $10^{10}$ translates into a coherent flux of $4.5 \times 10^{16}$ ph/sec inside the train or an average coherent flux of $2.7 \times 10^{14}$ ph/sec at $10^{-5}$ BW. The corresponding number at a forefront synchrotron source is ~ $10^5$ times lower.*

The start of commissioning and operation of the MID station is defined by the completion of the linac, undulators, and photon transport systems, including the main building in Schenefeld that will host the scientific instruments, laboratories, and offices. This building is expected to be ready in 2014 and commissioning of the linac and the X-ray beam transport is expected to begin in 2015. The MID instrument will be located at the central branch of the SASE2 beamline, where one of the side branches has been assigned to High Energy Density (HED) matter investigations. The second side branch will not be occupied in Phase I, but sufficient space needs to be reserved for later use.

---

[2] E.A. Schneidmiller and M.V. Yurkov, "Photon beam properties at the European XFEL", XFEL.EU TR-2011-006 (2011)
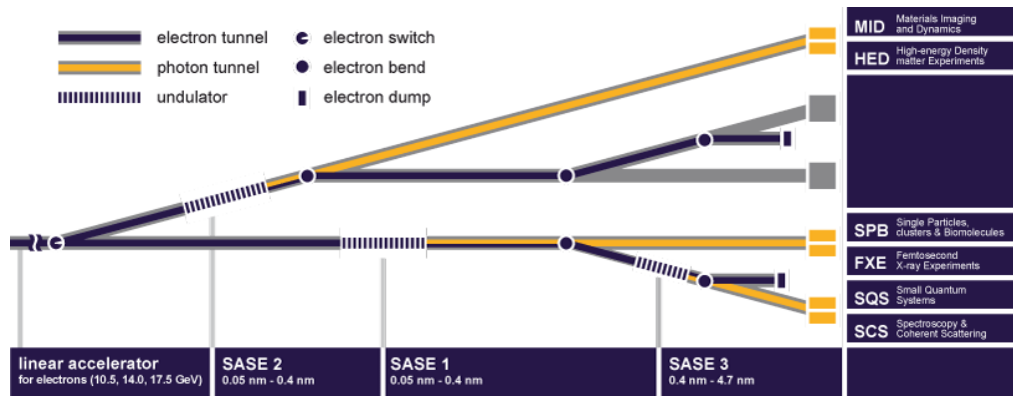
**Figure 3:** *Sketch of the system of tunnels spreading out from the end of the linear accelerator.[3] Three separate undulator tunnels contain the SASE1, SASE2, and SASE3 undulators. In Phase I, six experimental stations are foreseen located at the end of three different photon tunnels as indicated. In an eventual second phase, more undulators can be installed and all five photon tunnels can be utilized. Eventually, every photon tunnel can feed up to three experimental stations, and, hence, 15 stations in total can be accommodated at a fully developed facility.*

---

[3] http://www.xfel.eu/research/beamlines/

# Science case

The science case for the European XFEL was first addressed in Chapter 6 of the *European XFEL Technical Design Report* (TDR) [1] and later discussed in a series of workshops on the various instruments foreseen. The workshop for the Materials Imaging and Dynamics (MID) scientific instrument took place on 28–29 October 2009 at ESRF in Grenoble [2], in particular addressing the scientific goals and requirements for X-ray Photon Correlation Spectroscopy (XPCS) [3] and Coherent X-ray Diffractive Imaging (CXDI) experiments [4]. This CDR builds on the aforementioned TDR and the XPCS report from the MID workshop [5] with the aim to detail the science case and the MID baseline layout, including the critical beamline components.

The idea behind the MID instrument is to offer the possibility to perform experiments with coherent X-ray beams of unprecedented intensities and at energies and timescales that never before have been available at storage ring sources. The coherent fraction of the beam intensity delivered by an undulator at a synchrotron is

$$\frac{I_C}{I} = \frac{\lambda^2}{\varepsilon_x \varepsilon_z (4\pi)^2}$$

(1)

where $\varepsilon_{x,z}$ denote the emittance in the horizontal and vertical directions, respectively. Only for sources that are close to being diffraction limited (i.e. $\varepsilon \sim \lambda/2\pi$) in both directions will this fraction be close to unity.

At most modern, third-generation synchrotrons (PETRA III, SPring-8, APS, ESRF) the coherent fraction is of the order $10^{-4} - 10^{-3}$, typically leaving a maximum of $10^{10} - 10^{11}$ coherent photons per second for experiments performed at 1 Å wavelength.

For SASE radiation at an XFEL, not only are there far more photons to begin with due to the microbunching of electrons in the undulator leading to the laser-like amplification, the coherent fraction is also much higher, as shown in Figure 4. For instance, at 8 keV, the coherent fraction is > 90% for all bunch charges considered (up to 1 nC), and the coherence remains good even at

higher photon energies. This leads to approximately a factor of $10^5$ gain in average coherent flux compared to third-generation synchrotron sources (see also Figure 2).
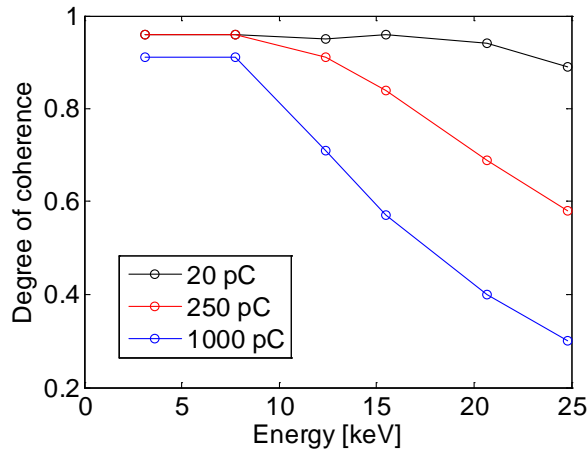


**Figure 4:** *Plot showing the degree of coherence vs. photon energy for different bunch charges (figure based on simulations by Schneidmiller and Yurkov [6])*

# Dynamics

Accessing the nano-structure of condensed matter with high time resolution is one of the primary goals of the MID instrument. This will be possible i) through conventional X-ray scattering experiments with high time resolution where ultrafast kinetics is accessible and ii) by taking advantage of the outstanding coherence properties of the SASE radiation enabling unmatched XPCS experiments. Structural dynamics will become accessible down to 220 ns (in multi-exposure mode) and down into the ps regime by employing split-delay techniques or by special linac filling patterns. Clearly, single-shot (diffract-and-destroy) experiments are of limited interest for dynamics investigations, except maybe in split-delay mode if an identical sample can be brought in easily and the damage happens at timescales longer than the delay[4]. The scientific motivation for XPCS at a free-electron laser source was first outlined in the TDR for the European XFEL [1] and detailed in a publication by Grübel et al. [7]. The main driving force is the potential to

---

[4] See extended discussion on pages 21–24 and 46–49.

access complex dynamics at the nanoscale far beyond what is possible today. Complex nanoscale dynamics is a ubiquitous phenomenon of fundamental interest at the forefront of condensed matter science, and comprises a multitude of processes, for example, visco-elastic flow and dissipation in liquids and glasses, polymer dynamics, protein folding, crystalline phase transitions, ultrafast spin transitions, domain wall dynamics, and magnetic domain switching. The timescales of interest range from femto-seconds to seconds. XPCS studies of sub-second dynamics in disordered systems at large momentum transfers were challenging up to now, and, for ultrafast processes (nano-seconds and faster), only inelastic scattering techniques, operating in the energy domain, could reveal the dynamics. This picture will change with the European XFEL source providing extremely brilliant (peak: $B > 10^{33}$; average: $B > 10^{25}$ ph/s/mm$^2$/mrad$^2$/0.1% BW) and highly coherent X-ray beams with a suitable time structure. Hence, for the first time, it will be possible to study (ultra)fast dynamics in the time domain giving direct access to the dynamic structure factor $S(q,t)$. This is essential for phenomena where time-averaging cannot be tolerated, for instance, non-equilibrium dynamics initiated by a pump pulse (pump-probe XPCS) or during a phase transition. In these cases, $S(q,t)$ change during the measurement and time-resolved information is required. The dynamics studies at the MID station will include glassy systems and liquids, surface dynamics, materials displaying quenched disorder, non-equilibrium and heterogeneous dynamics, magneto-dynamics, and ultrafast kinetics studies in small- and wide-angle scattering geometries. Selected experiments that are believed to be archetypical for the window of opportunity that the MID station will open are detailed below.

## Glassy dynamics

When rapidly cooled below the freezing point, most liquids organize in meta-stable glassy or amorphous phases. This picture applies for a broad range of materials, including organic liquids, metallic alloys and oxides, polymeric materials, and many others. XPCS measures the time constants of a system as a function of wave vector q and gives direct information about the dynamic properties through the decay time and shape of the correlation functions. The

region of q and time that can be covered is essential for the experiments, and, with the significant gain in coherent flux compared to today's most powerful SR sources, these experiments can be taken into a new regime. Studies will span a wide range of timescales, from $10^{-12}$ to $10^3$ s, in order to observe the evolution of the dynamics from liquid to glassy behavior as the temperature is changed. In order to cover this broad range in time, different experimental strategies need to be applied. Timescales longer than 220 ns are reachable in sequential XPCS taking advantage of the spacing between pulses in a train or even by correlating frames from different trains. Faster dynamics is either accessible through split-delay techniques (ultrafast split-delay XPCS) or could be feasible by operating the linac in custom modes where electron bunches with smaller separation could be generated (down to ~ 800 ps).

Thanks to the great simplicity of their metallic bonding based structure, metallic glasses can be viewed as ideal candidates to shed light on the glass transition phenomenology and, in particular on the behaviour of the structural relaxation time, or the viscosity, upon approaching the glass transition temperature $T_g$ from the supercooled liquid phase. More conventional glass formers, such as molecular or polymeric systems or soft glassy networks, are characterized by intra-molecular, re-orientational, and translational molecular motions that can screen the intrinsic physics of the glass transition. Since the first bulk metallic glasses (BMG) appeared in the 1980s, a strong effort has been made to characterize this new class of materials. Due to the lack of long-range ordering and hence the absence of lattice defects in the amorphous state, the mechanical response and transport properties of BMGs cannot be treated in the framework usually employed for crystalline materials. At the microscopic level, the mechanical response of BMGs is controlled by inter-atomic forces between randomly distributed atoms and dynamical studies in the liquid and glassy states provide the most direct way to gain insight into these fundamental interactions.

Recent XPCS experiments at ID10A, ESRF indicate that only a limited range of dynamics can be captured in such systems at synchrotron radiation sources. The incident partially coherent beam has an intensity of about $10^{10}$ photons/s and, under these conditions, only very slow dynamics (~ 5 s or slower) can be tracked neat $T_g$. Also, one is restricted to working at the peak of S(q) as the scattered intensity falls of rapidly in q. At the European XFEL it

will be possible to follow the structural dynamics on much faster timescales and over a much broader q-range. Moreover, the statistics will be so good that the angular correlations [8], revealing short-range ordering and local symmetries in otherwise disordered systems, can be time-resolved at least on the 220 ns timescale within a pulse train—if the detector size and speed allow it. To gain access to faster times than given by the bunch train structure, split-delay XPCS can be employed. Here, the speckle pattern is integrated over two pulses, and the spacing between the pulses (delay) determines the accessible time scales. Delays may be created in the linac or by split-delay lines, and the ps-to-ns range should be accessible. Importantly, in the split-delay mode, the time resolution is decoupled from the detector speed but encoded in the images via the delay. This is fundamentally different from the sequential mode, where the detector speed determines the time resolution and ideally must be matched to the pulse train structure (4.5 MHz rep. rate).

Also for organic molecular glassformers the European XFEL will offer new possibilities. The dynamical processes responsible for the dramatic slowdown of molecular motion upon supercooling and subsequent vitrification below the glass transition temperature $T_g$ lack an unified explanation. Mode-coupling theory [9] is one of the most successful concepts that quantitatively predicts many features of the supercooled liquid-to-glass transition [10] up to the crossover temperature $T^* \sim 1.1$ - $1.6 \cdot T_g$. For most glass-forming liquids, the temperature dependence of the relaxation time $\tau$ below $T^*$ can be well described by the Vogel-Fulcher-Tammann (VFT) expression $\tau = A \exp[B/(T-T_{VF})]$. Measurements of $\tau$ are usually obtained by dielectric spectroscopy (DS) or mechanical spectroscopy (MS). These techniques measure the relaxation of a macroscopic parameter that then can be related to the nanoscopic dynamics under certain model assumptions. However, access to direct measurements of the length-scale resolved molecular motion is essential, in particular when it comes to larger organic molecules where several modes can be involved leading to a very complex dynamical behaviour.

Experiments from ESRF show that in the best cases dynamics on the order of a few seconds can be quantified in organic systems at scattering vectors corresponding to inter-molecular distances. Typically, XPCS covers a time window that is not accessible by DS or MS but unfortunately the XPCS data

cannot overlap with these techniques due to the limited coherent flux preventing access to faster times. Numerous dielectric studies clearly indicate a broad distribution of relaxation times near $T_g$, and hence a stretched exponential correlation function $\sim \exp(-2[t/\tau]^\gamma)$ with $\gamma < 1$ would be expected as well as a strong temperature dependence of $\tau$. Surprisingly, in these systems, the correlation functions often show simple exponential decays ($\gamma = 1$) and very weak temperature dependencies. Hence, it appears that the relaxation of dipole moments (measured by DS) and the translational molecular diffusion (measured by XPCS) display quite different behaviours near $T_g$. Unfortunately, due to the limited coherent flux even at the most powerful third-generation synchrotrons, a systematic study of this effect above $T_g$ is impossible. Here, the XFEL would offer exciting new possibilities with both sequential and split-delay XPCS. Both diffusive dynamics and angular correlations could be tracked at micro- to pico-second timescales unravelling the molecular dynamics in organic glass formers.

# Surface and interface dynamics

The investigations of surface, or near-surface, dynamics is another field where the large coherent flux of the European XFEL will lead to scientific breakthroughs. X-rays are ideal for surface-sensitive measurements thanks to the evanescent wave that travels parallel to the interface with very limited penetration depth when the X-rays are applied at a grazing angle of incidence (smaller than the critical angle for total external reflection). On the other hand, the difficulty in surface X-ray scattering is caused by the small amount of material that is probed when the penetration depth is on the order of $\sim 10$ nm. Until now, measurements of free surface dynamics have been performed only in the strong diffuse scattering region very close to the specular reflection $q_{\parallel} \sim 10^{-6} - 10^{-4}$ Å$^{-1}$ [11, 12] or at in-plane correlation peaks, e.g. originating from nano-particle tracers with large density contrast floating on the surface (see refs. [13, 14]).

With the European XFEL beam, it will for the first time become possible to study surface and interface dynamics at the atomic and molecular scale by X-ray scattering. In addition, the option to perform XPCS at photon energies

up to 25 keV (or higher) opens up the possibility to probe dynamics at buried liquid–liquid and liquid–solid interfaces. For instance, at 25 keV, it is possible to penetrate 2 mm Si or 23 mm of $H_2O$ (1/e absorption length). Going to 30 keV, this number grows by more than 50%. Self-organization, self-assembly, and growth of nano-particles could be followed by coherent X-ray scattering, allowing kinetics and dynamics studies of such processes at interfaces with unprecedented time resolution.

The liquid-gas interface is also of interest. For instance, the surface glass transition could be followed in grazing incidence geometry at high q probing only the near surface region, e.g. of a molecular glass-former like DC705 discussed above. The behaviour of the relaxation time vs. temperature or pressure can be tracked and compared with the bulk behaviour, yielding direct evidence about a possible surface glass transition. Previous XPCS experiments have attempted to address the question of a surface glass transition (see e.g. ref. [15]), but mostly indirect or inconclusive information was obtained. Solid substrate supported polymeric thin films were also probed [16, 17] but influences of substrate interactions and wetting properties [18] can easily shadow the true glassy dynamics. With the flux of the European XFEL, one can expect to approach the nano-scale limit for hydrodynamics where the usual continuum assumptions, e.g. resulting in capillary wave dynamics, will break down. However, there have been only very few observations of this transition.

Solid surfaces present a wealth of interesting phenomena that are relevant to study, for instance, the de-wetting of metallic thin films and the aggregation and coalescing dynamics that follows. The *in situ* growth and diffusion of nano-particles on reactive solid surfaces play an important role for many catalytic processes, and the MID setup will ensure that user-specific sample environments can be hosted to perform surface chemistry and catalytic experiments under realistic reaction conditions. Phase transitions, critical phenomena, and critical dynamics can also be measured at the surface of solids [19], for instance, order–disorder phase transitions in binary metallic alloys where a great deal is known about the bulk kinetics and dynamics [20–22], but almost nothing about how the dynamic properties change in the near-surface region. This is also true for measurements of phonon dispersions in liquid or crystalline materials where only a few attempts have

been made to address the surface/interface-specific properties directly [23]. All these types of measurements could be made in XPCS mode under grazing incidence conditions at the European XFEL to unambiguously probe the influence of the surface.

# Non-equilibrium and heterogeneous dynamics

Recent XPCS research has focused on the microscopic dynamics in disordered soft solids, e.g. colloidal gels, polymer gels, and concentrated emulsions where pronounced deviations from simple diffusive dynamics are observed, see ref. [24] and references therein. Specifically, a surprising finding of this work, and of related dynamic light scattering (DLS) experiments, has been the observation of compressed, faster-than-exponentially decaying correlation functions. An accompanying feature is a relaxation time that varies approximately linearly with the inverse of the wave vector, $\tau \propto q^{-1}$, implying hyper-diffusive, convective-like motion. The wide assortment of soft materials displaying these dynamics, as well as their observation with XPCS in a variety of polymeric systems and in colloidal dynamics in glassy solvents [25, 26], suggests a generic underlying mechanism; however, no clear consensus about their microscopic origin has emerged.

Often, a characteristic feature of these disordered soft solids is their out-of-equilibrium behaviour, which can complicate the analysis of XPCS measurements. In this case, the correlation analysis must be performed explicitly as a function of time, or "age", and the time averaging of the correlation function is replaced by an ensemble averaging leading to a two-times correlation function [27]. This approach necessitates the use of an area detector with high spatial resolution where symmetries in the scattering pattern, such as the azimuthal symmetry of scattering from an isotropic system, can be exploited to collect intensity measurements simultaneously at many equivalent pixels. The European XFEL is in a good position to push the investigations of complex, non-equilibrium dynamics further. Several systems, including clays and colloidal- and polymer gels [28–30], investigated to date display multiple relaxations where the faster dynamics only is indirectly visible. The boost in coherent flux with the advent of XFELs will allow

recording time-resolved correlation functions that are not accessible with today's X-ray sources and obtain 220 ns time resolution in sequential mode two-times XPCS. Possibly, the two-times scheme can also be extended to the ultrafast XPCS mode with the split-delay technique.

Deviations from Gaussian statistics in the fluctuations of the two-times correlation functions can be used to determine if the dynamics is heterogeneous. This is for instance the case in jammed systems with arrested dynamics that is characterized by an intermittent dynamic behaviour. Calculation of higher-order time correlation functions is the most direct way to quantify dynamical heterogeneity, but, at present, this is very challenging due severe signal-to-noise limitations in most data sets and has consequently only been possible in a few cases. With the greatly improved s/n ratio in mind, this could become a standard technique at the MID station.

## Ultrafast coherent scattering and XPCS

One of the methods suggested to achieve higher time resolution in the previously described experiments, i.e. beyond the timescale given by the repetition rate and the detector (4.5 MHz), is to modify the time structure of the pulse pattern that illuminates the sample. Here, we detail this idea and the applications further.

As described earlier, access to ultrafast timescales may be achieved by application of split-delay techniques where a pulse is separated into two parts by a 1:1 beam splitter (thin Bragg crystal or mirror) and a time delay is introduced between the two pulses. This can be realized by a difference in path length travelled by the two pulses that afterwards are brought back to be co-linear before they hit the sample with a corresponding time difference. Split-delay lines operating with Bragg crystals [31] or grazing incidence mirrors have been successfully tested in the past and a crystal-based device is currently installed and under commissioning at LCLS. Another strategy is to modify the bunch pattern directly in the linac where, under certain circumstances, it is possible to generate pulses separated by down to 0.8 ns within a train.

When two pulses hit the sample and scatter into the detector with a time difference less than 4.5 MHz, the detector will record a sum of two speckle patterns. This double-exposed detector image can then be analysed in terms

of its contrast, for instance, using speckle visibility techniques [32], spatial auto-correlations [33], or intensity histograms [3], with the potential to obtain a time resolution in XPCS of sub-ns or smaller. This method will allow pushing the fast limits of XPCS, and the split-delay line technique is in principle only limited by the duration of a pulse that can be in the range of 1–100 fs. The split-delay lines have limitations when it comes to generating delays in the few ns range and longer, and here the MID station relies on the possibility to generate these delays directly in the linac.

Looking into processes such as ultrafast demagnetization [34], investigations of frustrated ferromagnetic compounds ("spin ice") [35], and interplay between spin-orbital and ordering fluctuations [36–37], e.g. in complex metal oxides, will in most cases require split-delay XPCS due to the fast timescales of interest. Traditionally, such experiments have been performed by inelastic X-ray or neutron scattering, but often either the timescales are in the 1–100 ns range, where inelastic techniques have difficulties due to the required energy resolution, or detection in the time domain is simply preferred, e.g. to study non-equilibrium dynamic behaviour and non-Gaussian fluctuations.

Ultrafast XPCS is interesting for all liquid systems, e.g. to resolve the central quasi-elastic scattering peak, and this of course also applies to the previously mentioned glass formers at high temperatures where they are liquid. It is important to stress that the sample need not survive many such double illuminations in split-delay XPCS; one is enough as long as the damage happens at a time scale longer that the delay. In this case, statistics can be accumulated, for instance, if the liquid sample is continuously flowing through the beam and beam damage effects avoided in the correlation functions.

An example of the need for ns–ps resolution in soft-matter XPCS is shown in Figure 5. The sample is a cross-linked polymer gel with an ergodicity restoring terminal relaxation that can be followed by time-resolved XPCS at a storage ring source [30] (data from ID10A, ESRF). From the q and time variation of the contrast of the correlation functions, it can be deduced that there must be a faster relaxation present responsible for a partial decay. However, the process is out of the detection window, due to limitations in detector speed and coherent flux. This process is strongly time-dependent and hence techniques like neutron-spin-echo cannot reveal the dynamics due

to the long data acquisition times required. Split-delay XPCS could reveal this dynamics (marked with "?" in Figure 5), and, by the shape and q-dependence of the correlation functions, for the first time give direct information on the changes in molecular dynamics that eventually lead to the gel state.
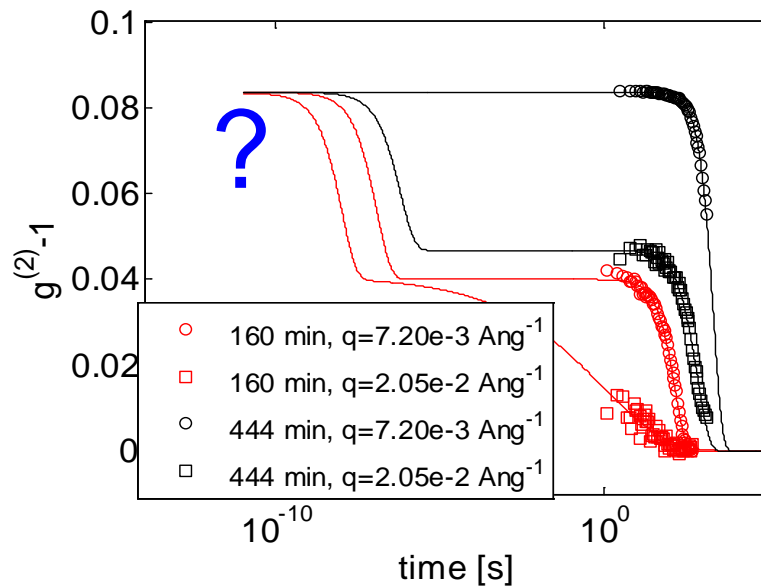


**Figure 5:** *XPCS data showing the time and q-dependence of the correlation functions of a cross-linking polymer gel. The solid lines are fits assuming the existence of a faster relaxation due to harmonically-bound-Brownian-particle (HBBP) motion of nano-sized polymer clusters. Data by Czakkel and Madsen [30].*

One of the main goals of the MID station is to enable all the kinds of XPCS experiments described above (sequential and split-delay), taking full advantage of the huge coherent peak flux of the European XFEL. The limitations in the timescale that can be reached and the samples that can be studied are of a technical nature (detector, machine jitter, stability) and also related to the radiation hardness of the samples. In all the cases described above where initial synchrotron experiments have been performed, the radiation hardness was not limiting the experiments, so it is clear that with the European XFEL a new window of opportunity will open for XPCS.

## Fast and ultrafast scattering: SAXS and WAXS

Thanks to the huge flux and the distinguished time structure, the European XFEL will also be interesting to use for "regular" time-resolved scattering experiments and investigate kinetics via time-resolved scattering. For this reason, the baseline MID instrumentation will feature a multi-purpose

SAXS/WAXS chamber that can host smaller setups, e.g. stop-flow devices, small cryostats, high-precision scanning stages, and sample environments for high-speed tomography or imaging. Such studies are today successfully carried out at third-generation synchrotron sources, but with the constant need for more flux to study faster processes and weaker signals, it is anticipated that these communities also will be attracted by the improvements offered by the European XFEL.

A particular research area that could open thanks to the European XFEL is *in situ* studies in the nano- and microsecond range of diffuse scattering, for instance, linked to catalytic surface activity. Likewise, the study of nano- and microsecond kinetics in soft-matter systems, e.g. related to reaction dynamics or self-assembly, is today very difficult in dilute samples. Such activities cannot be categorized as ultrafast science, nor do they rely on the coherence properties of the beam, but the respective scientific communities are very large with interesting scientific challenges and topics that often are close to industrial applications.

## Other dynamics

Mössbauer spectroscopy also has the potential to benefit from the time structure and high flux of the European XFEL. The employment of fast Avalanche Photo-Diode (APD) detectors is required and, as such, experiments could be performed with the MID baseline instrumentation foreseen for scattering experiments. A photon energy range from 5 to 25 keV will cover commonly used Mössbauer transitions in 57-Fe, 119-Sn, 151-Eu, 169-Tm, and 181-Ta. With an extension of the photon energy range e.g. up to 100 keV by use of a diamond Laue monochromator, more elements (e.g. Ni, Cr, Ag, and Au) could be included. Since 57-Fe is the most commonly used Mössbauer element, the MID beamline will feature the transition energy 14.4 keV as one of its main operating energies with optimized focusing capabilities. However, eventual requirements to an energy resolution better than $10^{-5}$ (e.g. provided by a high-resolution backscattering monochromator) will not be part of the MID baseline instrumentation.

The study of angular correlations and their time dependence does not require coherent photons but rather that only a limited number of scatterers are being illuminated. The angular correlations allow us not only to reveal hidden local

symmetries, e.g. in the short-range ordering of glasses [8], but also to study form factors of suspensions of macromolecules in solution scattering [38]. The MID station will offer the possibility to perform measurements of angular correlations and their time-dependence with unprecedented time resolution. This is described in more detail in the following section.

# Imaging

Coherent imaging techniques, which were identified in the European XFEL TDR as one of the key areas of targeted research, will play an important role at the European XFEL. At the MID station, Coherent X-ray Diffractive Imaging (CXDI), which shares many of the technical constraints that also apply to XPCS (e.g. concerning coherence requirements) will be at the focus. CXDI "diffract-and-survive" experiments have similar requirements for avoiding radiation damage as sequential XPCS and multiple exposure data acquisition on one single sample is often the goal. Diffract-and-survive CXDI enables 3D data to be taken if the sample can be rotated in between the exposures and techniques like ptychography [39, 40] or hard X-ray holography [41, 42] can be applied to extend the field of view and ease the convergence of the iterative phase-retrieval algorithm. Today, almost all hard X-ray CXDI experiments are limited by the coherent flux, the signal-to-noise, and the coherence properties of the radiation, and it can be anticipated that the European XFEL will lead to new breakthroughs in imaging of nano-structured materials science and biological specimens.

## Biological imaging

The imaging of biological material can be challenging due to the fragility and radiation sensitivity of the samples, their low-density contrast, combined with the need for 3D resolution. In particular, 3D imaging of living cells in the natural hydrated state is difficult [43, 44]. So far, the method of choice has been cryogenic Transmission Electron Microscopy (cryo-TEM) on samples that can be sectioned and stained to increase the contrast. The community has been looking for alternative methods and recently coherent diffractive X-ray imaging (aka X-ray diffraction microscopy) has appeared as a promising technique [45]. Impressive results have been obtained at

synchrotron radiation (SR) sources demonstrating that high-quality images can be obtained without sectioning and staining, but the images are still not matching the best cryo-TEM work in terms of spatial resolution.

Biological CDI at the European XFEL has the potential to take the technique further and obtain unmatched spatial resolution, e.g. in 3D cell images obtained by a tomographic reconstruction. The goal is to resolve subcellular organelles and structural details of the nucleus and the cell walls. The maximum sample size is determined by the detector resolution and the required degree of over-sampling of the speckle pattern. It is estimated that isolated structures of up to 3–5 $\mu$m could be imaged with a one-megapixel (1 Mpx) detector with 200 $\mu$m pixel size at the MID beamline. The resolution depends on the number of detector pixels—the more the better. For this type of experiments, it is essential that the transverse coherence properties of the individual pulses are uniform, or at least well known. Other areas of research that have been less explored until now at synchrotron sources, but could open up thanks to the power of the European XFEL, are 2D crystallography [46] and high-resolution, Fourier-transform bio-holography, as described in more details below.

An important example of new imaging experiments that could be carried out at the XFEL is provided by proteins that cannot be crystallized in usual 3D crystalline structures. For the first time, diffraction experiments on single 2D protein lattices could be possible and calculations suggest that radiation damage effects can be avoided in single-shot experiments with 1 to 20 fs pulse duration, even on non-frozen lattices in their natural wet environment. One protein of particular interest is the retinal bacteriorhodopsin (bR), also known as Purple Membrane (PM). By taking diffraction maps at different orientations, these experiments will demonstrate that high-resolution 3D protein structures can be obtained from 2D lattices. Structures from 3D crystals of the ground state and all the intermediates in the bR photo-cycle have been solved to beyond 3 Å resolution [47]. However, infrared spectroscopy has indicated that the conformational changes of the functionally important M2 intermediate are drastically reduced due to crystal packing effects. Electron microscopy (EM) on 2D PM lattices could in principle solve this question, but these experiments have turned out to be extremely difficult, even using the cubic phase crystallization method [48], and

have not been successful so far. Single PM lattices, typically 0.5 µm in diameter, can be deposited in large arrays on thin SiN membranes and made visible in a fluorescence microscope by use of a fluorescent dye. At every tilt angle a new lattice is positioned into the beam so that the diffraction patterns are rotated randomly with respect to each other, but the rotation angles can be determined if many different tilt angles are measured and phasing of the diffraction patterns can be achieved by molecular replacement. The advantage of this new methodology is that high-resolution 3D structures of ground and intermediate states of single proteins can be obtained from 2D lattices in the non-frozen state and in a more natural environment. This avoids systematic errors due to 3D crystal packing effects that have appeared as a limiting factor in crystallography of intermediates.

Coherent radiation from X-ray free-electron lasers (FELs) also provides the unique opportunity of imaging biological objects using holographic techniques. In particular, single pulses in the range of 1 to 100 fs with an extremely high number of photons per pulse will allow us to image single macromolecular complexes. Living cells use a large number of complexes for efficient multistep processes and in modern structural biology, complexes of cellular components are in the focus of research.

The advantages of using SASE radiation for imaging of complexes are the following:

**(i)** By using short X-ray pulses, radiation damage can be avoided as the extremely high number of coherent photons per pulse allows single-shot imaging of a single complex before destruction.

**(ii)** This provides the unique possibility to study single biological objects in a wet unfrozen state in their natural environment.

**(iii)** Holographic imaging in combination with phase retrieval methods will lead to increased resolution.

Holographic imaging experiments on inorganic and cellular objects using soft and hard X-rays have been demonstrated previously [41, 42, 49–51]. Experiments in which this concept is adapted to XFEL radiation can be foreseen in imaging of complexes and, for instance, the ribosome from *E. coli* could be studied. A gold sphere can be fixed to the ribosome by a strand of

DNA and the whole assembly sprayed into the X-ray beam using an aerosol injector that has proven to be efficient in FEL scattering experiments on small biological objects. Fourier transform holograms of thousands of these particles need to be analysed and the images classified with respect to the different orientations. Ribosomes are ideal test objects for the imaging of complexes since, in the past, their structures have been investigated by small angle neutron and X-ray scattering giving low-resolution data, by electron microscopy to yield medium resolution, and by 3D crystallography with high resolution. In addition to the readily available holographic reconstruction (inverse FFT), one can use iterative phase retrieval in a second step to increase the lateral resolution as demonstrated by Stadler et al. [41]. Large membrane protein complexes that are difficult (impossible) to crystallize, including those from the respiratory chain or photosynthetic complexes, could also be imaged. In test experiments at synchrotron sources, gold spheres of a few 100 nm had been used to create the reference wave in 3D imaging. In XFEL experiments, the size of the reference object can be downscaled to 2 nm, hence promising a better resolution and eventually the use of uniformly redundant arrays could be foreseen whenever possible [51].

## Imaging in nano-science

CXDI in nano-science, pioneered by I. K. Robinson and co-workers for the Bragg case, was used to visualize the interior of nano- and micron-sized materials science samples [52–57] using iterative phase retrieval algorithms on oversampled diffraction patterns. Later, technical developments using holographic and ptychographic methods have been achieved, as described above. Recently, it was proposed by Miao and co-workers [58] that 3D information from an isolated object can be extracted from a single (or a few) 2D projection using the so-called ankylography technique when the coherent diffraction pattern is sufficiently oversampled on the Ewald sphere. Like traditional CXDI, ankylography benefits from a detector with many pixels that ideally should measure intensities equidistantly on the Ewald sphere (spherical detector), see Figure 6, and cover as large a q-range as possible. Alternatively, the Ewald sphere curvature can be reduced by going to higher photon energies and a plane detector used. Given these requirements, and the need for a small bandwidth ($\Delta\lambda/\lambda < 1/(n\,\Omega)$) where n is the number of resolution elements and $\Omega$ the over-sampling ratio, this technique fits well with

the capabilities of the MID instrument. However, the extent to which the structure of "real" 3D samples (that also are thick along the direction of propagation) can be correctly rendered by single shots is still under debate and a multi-exposure scheme seems unavoidable.
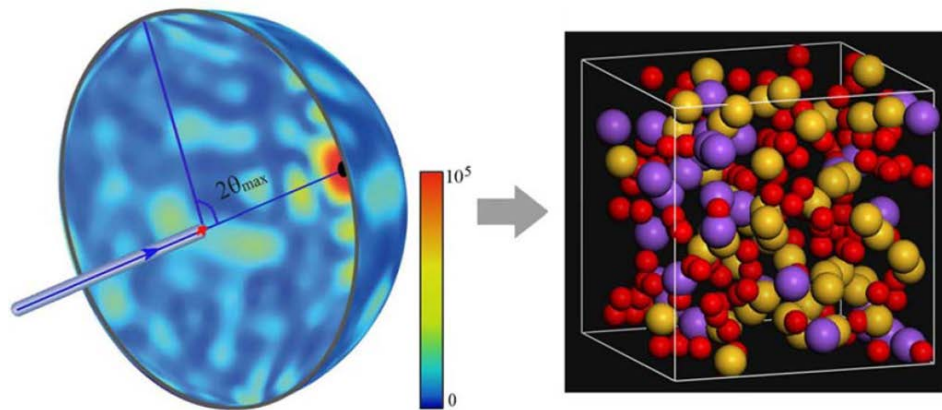


*Figure 6: Illustration of an X-ray diffraction imaging setup where the scattering from a disordered model system, a Sodium silicate glass (right), is sampled on the Ewald sphere. Depending on the oversampling ratio, the maximum scattering angle, the sample geometry, and the X-ray bandwidth, 3D information with atomic resolution is, in principle, accessible from one view by using iterative phase retrieval. Figure adapted from ref. [58] by J. Miao et al.*

Coherent diffractive imaging on polycrystalline samples, that are typical in materials science, is not trivial, particularly if the goal is to approach atomic resolution. Using a combination of CXDI phase retrieval methods, e.g. the hybrid input-output algorithm, and indexing multiple Bragg spots by 3D diffraction methods [59] could be a possible way forward to address this problem [60]. The possibility to perform these experiments at the MID station with higher photon energies than previously available for coherent scattering techniques is of paramount importance in order to investigate samples of non-vanishing thickness. Together with the exploitation of the time structure of the machine, this will provide new possibilities for *in situ* CXDI studies in materials science on the ns–ms timescale, or even faster using split-delay techniques.

The calculation of angular correlations from scattering data is a method originally proposed about 30 years ago [38] to derive 3D molecular structures from solution scattering. Recently, the technique was rediscovered [7] and, for the first time, used to uncover local symmetries in glassy colloidal suspensions from scattering data, as shown in Figure 7. The frequent

occurrence of five-fold symmetries reflects that, while this structural arrangement can minimize the energy on the local scale, it of course prevents the formation of long-range ordering. Hence, these local symmetries may play a decisive role in stabilizing the glassy state. The possibility of revealing bond orientation order in molecular glasses [61], together with the prospects for uncovering fundamental aspects of the glass transition, is one of the main reasons why this technique will be pursued at the MID station. At high q, the scattering signals are weak and the flux of the XFEL is required. Needless to say, the combination with the high time resolution offered by the European XFEL is unique.
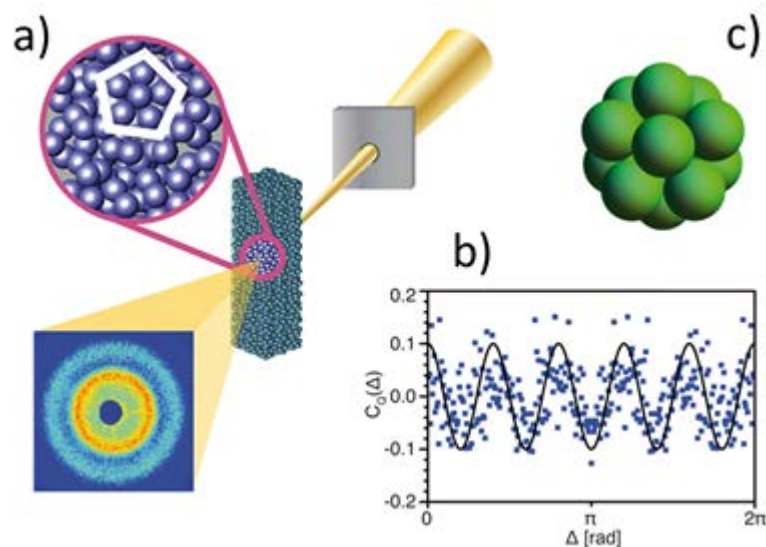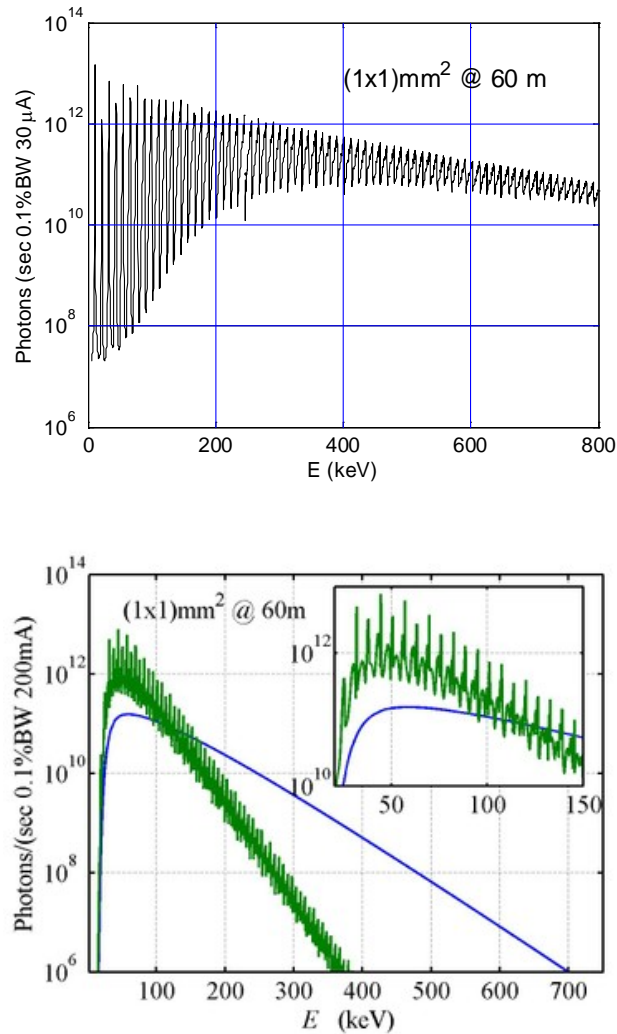


*Figure 7: a) Illustration of the setup used to measure angular correlations in a glassy colloidal suspension. b) Example of an angular cross-correlation function with five-fold symmetry. c) Model of a possible structural arrangement of a colloidal cluster with five-fold symmetry. Figure adapted from ref. [7] by P. Wochner and co-workers.*

# High photon energy experiments

The European XFEL will provide a high photon flux also above 25 keV, both via the third harmonics of the SASE and the spontaneous radiation. Beyond about 40–50 keV, the spontaneous spectrum (usual undulator radiation) is more intense than the SASE peaks. The average spontaneous flux (approximately estimated by use of the SRW package in IGOR, still needs to be taken with a grain of salt) is shown in Figure 8 and compared to the flux of

the ID15 beamline of ESRF, which today has one of the highest brilliances worldwide in the range 50–150 keV. At 60 keV, there is essentially no gain in average flux, while the XFEL intensity is about one order of magnitude higher at 150 keV. At 600 keV, the XFEL source is approximately $10^4$ times stronger than the wiggler source at ID15.

Looking instead at the Brilliance ($B_{max} > 10^{21}$ @ 160 keV) and the peak values, the spontaneous radiation from the XFEL undulator is even more favourable, which will result in a really superior performance with focused beams and in time-resolved experiments, also in the 50–150 keV range. Compared to today's best sources, this opens new exciting possibilities for high-energy scattering experiments in materials science. Such experiments require the use of a Laue double crystal monochromator instead of grazing incidence mirrors in the tunnel to get around the central stop and monochromatize the beam. In terms of Thomson scattering, the need for photon energies above ~ 150 keV is limited. However, one advantage of high energies could be the possibility of having the entire atomic form factor peak in the forward scattering direction (e.g. HWHM < 3 deg for most metals above 300 keV photon energy). That would open up for angular correlation measurements with atomic resolution using a reasonably sized (~ 1 Mpx) detector, and could be combined with the high time resolution intrinsic to the machine. Photon detection becomes increasingly challenging at higher and higher energies, and the total attenuation cross section does not decrease any more (1/e attenuation length stabilizes at about 1 cm for most metals above 150 keV) because Compton scattering takes over as the dominant photon–electron interaction. This poses a severe challenge to efficient photon detection at these energies that is not currently covered by the European XFEL detector program. Magnetic Compton scattering could possibly benefit from the very high flux at very high energies. Combination with pulsed magnetic fields is natural due to the AC nature of the source, but additional polarization control would be needed for magnetization studies.

*Figure 8:* *Calculations of the average spontaneous emission from a 175 m long undulator (40 mm period, K = 3.32, 13 pm emittance, and 30 μA average current, similar to the SASE2 undulator planned at the European XFEL) through a 1 x 1 mm² slit in 60 m distance (top) compared with the performance of ID15, ESRF (bottom). The blue and green curves show the performances of the wiggler and the U22 undulator, respectively [62]. More precise calculations of the spontaneous emission from the SASE2 undulator are in progress.*

Looking instead at the Brilliance ($B_{max} > 10^{21}$ @ 160 keV) and the peak values, the spontaneous radiation from the XFEL undulator is even more favourable, which will result in a really superior performance with focused beams and in time-resolved experiments, also in the 50–150 keV range. Compared to today's best sources, this opens new exciting possibilities for high-energy scattering experiments in materials science. Such experiments require the use of a Laue double crystal monochromator instead of grazing incidence mirrors in the tunnel to get around the central stop and

monochromatize the beam. In terms of Thomson scattering, the need for photon energies above ~ 150 keV is limited. However, one advantage of high energies could be the possibility of having the entire atomic form factor peak in the forward scattering direction (e.g. HWHM < 3 deg for most metals above 300 keV photon energy). That would open up for angular correlation measurements with atomic resolution using a reasonably sized (~ 1 Mpx) detector, and could be combined with the high time resolution intrinsic to the machine. Photon detection becomes increasingly challenging at higher and higher energies, and the total attenuation cross section does not decrease any more (1/e attenuation length stabilizes at about 1 cm for most metals above 150 keV) because Compton scattering takes over as the dominant photon–electron interaction. This poses a severe challenge to efficient photon detection at these energies that is not currently covered by the European XFEL detector program. Magnetic Compton scattering could possibly benefit from the very high flux at very high energies. Combination with pulsed magnetic fields is natural due to the AC nature of the source, but additional polarization control would be needed for magnetization studies.

Imaging studies in materials science at very high energies (200–1000 keV) could provide an interesting, high-resolution alternative to neutron imaging (neutron radiography or tomography) usually preferred for cm-thick metal samples (e.g. combustion engines, train rails, airplane wings), also in view of the possibility to combine it with the high time resolution that can be achieved at the European XFEL. Due to the demanding and expensive requirements for shielding, it is not foreseen to transport beams above 200 keV into the experiment hall. Hence, if pursued, these very high-energy experiments need to be undertaken in the photon tunnel upstream of the main beam stop and Bremsstrahlung collimator where space could be reserved.

# Technical considerations

This chapter describes some of the boundary conditions that are decisive for the success of the scientific program illustrated by the archetypical experiments outlined in the "Science case" chapter. In fact, these are rather fundamental requirements that turn out to put very specific demands on the XPCS and CXDI instrumentation, in particular concerning sample damage, the detection scheme, and the detector specifications. The importance of these requirements justifies including this chapter—which is of a rather technical character—in the CDR before the general outline of the beamline and instrumentation is provided in successive chapters. The main conclusions are summarized at the end of the chapter.

## Feasibility of XPCS: signal-to-noise ratio

This section addresses several issues concerning the technical feasibility of XPCS at the European XFEL. In particular, the question of whether the samples will be damaged or even blow up after the first shot will be treated here.

It is well known [27, 63, 64] that the signal-to-noise ratio (SNR) in sequential multi-speckle XPCS is approximately given by

$$\mathrm{SNR} = \langle I \rangle \sqrt{N} \sqrt{M} \, \frac{\beta}{\sqrt{1+\beta}}. \tag{2}$$

Here N is the number of detector pixels, each of size a $\times$ a, where M is the number of time bins, $\langle I \rangle$ is the average number of photons registered by a pixel during the time bin, and $\beta$ is the optical contrast.

This formula has the important and well-known consequence that one order of magnitude more intensity gives access to two orders of magnitude faster times. This is easily realized by noting that $\langle I \rangle = I_0 \, \tau_m \, (a/R)^2$, where $I_0$ is the total scattered intensity (photons/s, depends on the sample and the incident

beam strength) at the given momentum transfer q, $(a/R)^2$ is the solid angle extended by one pixel with R as the sample-detector distance, and $\tau_m$ is the binning time. The total acquisition time is $T = M \tau_m$, and hence we get for the SNR

$$SNR = I_0 (a/R)^2 \sqrt{N} \sqrt{T} \sqrt{\tau_m} \frac{\beta}{\sqrt{1+\beta}}. \tag{3}$$

Hence, if $I_0$ for instance is increased by a factor of 10, $\tau_m$ can be decreased by a factor of 100 keeping the same SNR.

The SNR depends on the beam and detector parameters as given in the above formulae. In general, the higher the number of counts per pixel the better, but there are important limitations to this simple picture. Indeed, the parameter $(a/R)^2$ suggests that large a and small R is better for the SNR. On the other hand, for a given $\Delta q/q$, N becomes larger if the detector pixels are smaller and the detector placed further downstream favouring large R and small a. The optical contrast also plays a role and pulls in the same direction where, in order to maximize $\beta$, it is better to have small a and large R. In addition, the optical contrast of the correlation functions is decisive for the experiments where a minimum $\beta$ is required; otherwise, effects like drift of the sample and fluctuation of the baseline, e.g. due to incorrect normalization or periodic errors, can be mistaken for sample dynamics.

It turns out that a discussion including SNR and sample damage is difficult to generalize and at least a differentiation according to the *q*-range (SAXS vs. WAXS) and the material under study (low Z vs. high Z) must be made. This is attempted below in an analysis where the temperature rise of the sample is taken as boundary condition.

### SAXS geometry

The optical contrast $\beta$ in the experiment, assuming a fully coherent beam of size d × d, is given by the complex degree of coherence convoluted with the detector resolution, and can be written [27] as

$$\beta = \left[ \frac{2}{w^2} \int_0^w (w - v) \left( \frac{\sin v/2}{v/2} \right)^2 dv \right]^2 \tag{4}$$

where w = 2πad/(λR) and λ is the wavelength. For maximizing the optical contrast, a small w is favourable, i.e. both small beam size d and small pixel size a is better. This requirement will be challenging to fulfil if the sample needs to survive the XFEL beam and with a pixel size of a = 200 μm. The dependence of β on w is shown in Figure 9.
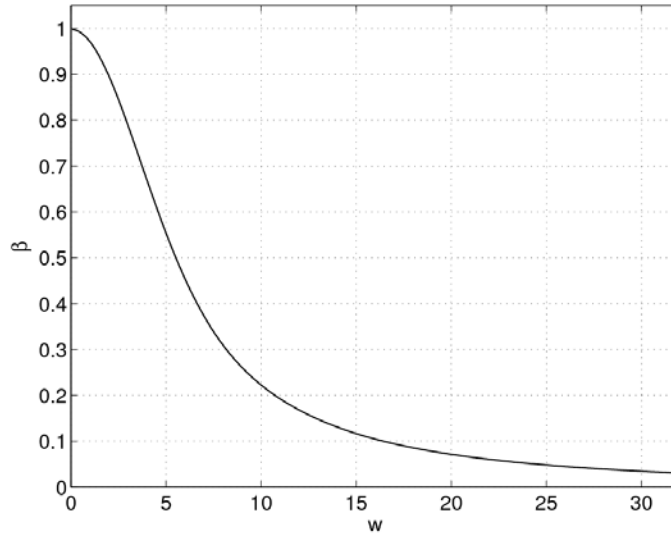


*Figure 9: Dependence of the optical contrast β on w (eq. 4).*

In SAXS geometry, the number of pixels in an annulus on the detector centred on the direct beam and with radius and width defined by q and Δq/q is

$$N \approx q^2 \frac{\Delta q}{q} (R\lambda)^2 / (2\pi a^2) \tag{5}$$

(assuming that the full annulus is covered by the detector) and we split into two cases:

**1. No focusing.** Then we can assume that $I_0$ is proportional to $d^2$ and S(q), the scattering factor of the sample, and we find from eq. (2)

$$SNR \propto S(q)q \sqrt{\frac{\Delta q}{q}} d\lambda^2 w\beta / \sqrt{1 + \beta}. \tag{6}$$

We note the trivial dependence on S(q), typically $S(q) \propto q^{-n}$, and the linear gain in SNR with d. Moreover, the SNR scales with $\lambda^2$. The last part of eq. (6), $w\beta/\sqrt{1 + \beta}$, is shown in Figure 10 and suggests a maximum in SNR at w ≈ 6,

meaning that a ≈ λR/d is the optimum working condition. This is a well know result for SAXS XPCS.
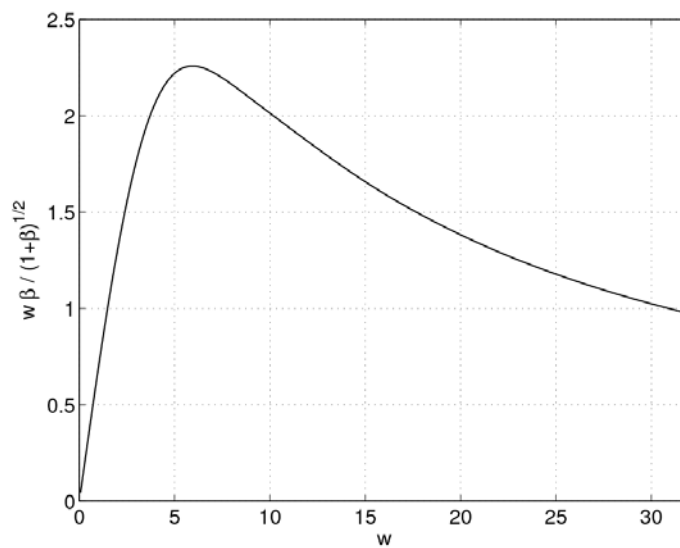


**Figure 10:** $w\beta/\sqrt{1+\beta}$ as a function of w showing a maximum close to w=6.

For a = 200 μm (value of the AGIPD detector), R = 5 m, λ = 1 Å, and d = 50 μm, we get w ≈ 125, and the SNR is down by a factor of 8 compared to the optimum case. Even more problematic is that the optical contrast β in this case is only 0.2%! These are obviously impossible working conditions. Moving the detector to R = 10 m does not help a lot; in this case, the SNR is down by a factor 4 with a contrast of 0.9 %. These are also very difficult working conditions.

From Figure 10 we determine that w should be in the range w ∈ [2 ; 26] for the SNR to be within a factor of 2 of the maximum attainable. This interval corresponds to β ∈ [90% ; 5%] for the contrast. For a given λ and d, the best SNR is achieved at β = 46% (see Figure 9). Working at w = 26 would be possible only by slitting down the beam (at least to d = 10 μm for R = 5 m), which again reduces the SNR, through the d dependence in eq. (6), by a factor of 5. In total, one order of magnitude in SNR is lost compared to the best case, essentially because a is very large. In this case, it would be interesting to work at λ = 2.48 Å (5 keV), which would give a factor of 6 better SNR than for λ = 1 Å, see eq. (6). For example, at 5 keV, w = 26 is achieved for beam size d = 25 μm with R = 5 m and a = 200 μm pixel size.

A more efficient way to reduce the beam size is by focusing, which we treat below.

**2. Focusing.** Then we can assume that $I_0$ is proportional to $S(q)$ but independent of d, and it will be bigger than $I_0$ in Case 1 above, at least for small d, where the total beam intensity is reduced significantly when focusing is not available. The SNR is then larger by a factor of ($I_{0, \text{ focus}}$ / $I_{0, \text{ no focus}}$) and proportional to

$$\text{SNR} \propto S(q)q \sqrt{\frac{\Delta q}{q}} \left(\frac{\lambda^2}{d}\right) w\beta / \sqrt{1 + \beta}. \qquad (7)$$

Not only is the SNR higher than in the no-focusing case but it also gets better with smaller d because the speckle size increases. For a given d, the condition $a \approx \lambda R/d$ still holds for the optimum SNR, or $w \in [2, 26]$ as defined earlier, and this condition gets easier to fulfil with smaller d. The $\lambda^2/d$ dependence of the SNR in eq. (7) suggests that minimizing d and maximizing $\lambda$ is the best strategy to take in lowering w. The obvious question is whether the sample supports the focused XFEL beam. When d cannot be made smaller (beam damage) and at the largest possible $\lambda$ (2.48 Å corresponding to 5 keV), w can only be reduced—and hence the contrast and SNR increased—by reducing a/R. This underlines that an absence of suitable XFEL detectors with small enough pixels make it tricky to work in the optimum w range, and that losses can be expected.

We conclude that focusing always should be used as it greatly improves the SNR and allows working with larger pixels. Beam damage should be managed by taking power out of the beam (monochromator, absorbers) upstream of the sample. In SAXS geometry, this strategy is much better than masking the detector pixels where photons are lost after the sample by the mask but still contribute to possible damages by hitting the sample. Figure 11 shows the behaviour of the optical contrast in SAXS for different beam sizes, at different photon energies, and with different detector pixel sizes assuming $10^{10}$ ph/pulse and R = 10 m. We estimate the maximum tolerable temperature increase in $H_2O$ to be 1 K per pulse and find that this is difficult to achieve with $\beta$ = 5%, which is the earlier determined minimum contrast. For Cu, the situation is even worse, in particular for 24 keV, which is above the K-edge. For fixed $\beta$, the calculations show that the beam size required varies linearly

with $\lambda$. This means that, in the case of water, where the temperature rises are almost identical for the different energies (see Figure 11 legend), the SNR for fixed $\beta$, e.g. 5 %, varies like $\lambda$ (due to the $\lambda^2/d$ factor in eq. (7)) and hence favours low energy operation. Figure 11 also illustrates that by keeping $\beta$ = 5%, the temperature rise is reduced by more than a factor of 15 if detector pixels of 50 $\mu$m size are assumed instead of 200 $\mu$m (example: $H_2O$ at 24 keV). Alternatively, $\beta$ = 46% and hence a maximum SNR could be attained with the same temperature rise ($\Delta T$ marked with *) with 50 $\mu$m pixels (example $H_2O$ at 5 keV). Operation above the K-edge in high-Z materials should be avoided as illustrated by the huge temperature rise for Cu at 24 keV.
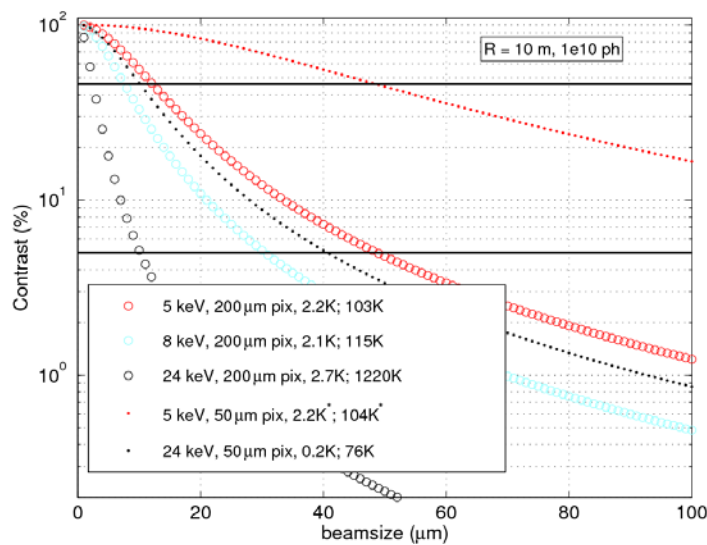


**Figure 11:** *Contrast vs. beam size at q = 0.01 $\mathring{A}^{-1}$ (SAXS regime). Two horizontal lines indicate the minimum contrast needed ($\beta$ = 5 %) as well as the maximum ($\beta$ = 46%) for the SNR factor in Figure 10. The two temperature numbers in the legend show temperature rises $\Delta T$ for $\beta$ = 5 % referring to $H_2O$ and Cu, respectively. The energy and material dependent 1/e attenuation length is used as sample thickness to evaluate $\Delta T$, but the contrast is not affected by that in SAXS geometry and hence the contrast vs. beam size curves are identical for Cu and $H_2O$. The $\Delta T$ marked with stars (*) are calculated for a SNR optimized contrast, namely $\beta$ = 46%.*

We conclude that, in SAXS geometry, the minimum energy and the maximum sample-detector distance R should be used. Due to other limitations in optics and available space, we estimate those limits to be around 5 keV and 10 m. Taking the pixel size as a fixed boundary condition, at least for the first version of the AGIPD detector that will be available in 2015 (a = 200 $\mu$m), we

find that a beam size of 50 $\mu$m will give 5% contrast, which is within a factor of 2 from the optimum SNR. Such beam conditions (assuming $10^{10}$ ph/pulse) will lead to a 2.2 K increase per pulse in water and 103 K for Cu, according to Figure 11. Even if the samples certainly can be brought to survive single shots and, in most cases, also diffract enough photons in a single shot for the XPCS method to work, obviously the data acquisition strategy needs to be adapted to ensure that the sample stays unperturbed throughout the entire illuminated time. A possible way forward could be to incorporate pauses without illumination where the sample is allowed to conduct heat to the environment or to continuously exchange the sample. More accurate models incorporating heat transport and convection are currently being investigated to outline a feasible data acquisition strategy. In SAXS geometry, the need for smaller pixels is particularly urgent for high-Z materials where attenuation otherwise will be required. As low-Z materials typically are more fragile, even a 2 K temperature rise may be too much and less than the $10^{10}$ ph/pulse can probably be accepted if the sample is to survive an entire pulse train. This makes split-delay XPCS particularly appealing as the sample needs to stay unperturbed for two pulses only. XPCS in SAXS geometry up to 24 keV is an interesting option (but staying below the K-edge is required in high Z materials) that requires smaller foci but would allow us to work with thicker samples, hence possibly reducing beam damage effects (the 1/e abs. length for $H_2O$ at 24 keV is 21 mm). Finally, it is worth remembering that the spectral purity $\Delta\lambda/\lambda$ does not enter the SNR expression in SAXS XPCS and, hence, in principle a monochromator is not needed. However, depending on limitations coming from the use of a monochromator (beam distortion, limited number of pulses transmitted, etc.) it can be seen as an alternative to "pink" SAXS XPCS where attenuation would be needed anyway.

## WAXS geometry

This geometry is more complex to analyse because the optical contrast depends on q in a non-trivial way, and because $\Delta\lambda/\lambda$ and the sample thickness h also enter the expression for $\beta$. Moreover, the speckle size is not necessarily uniform in the vertical and horizontal directions. To calculate $\beta$, we use the formalism developed by Jakeman and Pusey for DLS [63, 64], and later adapted to the X-ray case by Abernathy et al. [33], Falus et al. [65], and Sutton [66].

An iso-q annulus will typically not fit entirely in the detector, and the number of pixels N that can be used in calculating the ensemble averaged correlation function is defined by $\theta$ (half the scattering angle) and $\Delta\lambda/\lambda$ so

$$N \approx \sqrt{N_{tot}} \left(\frac{\Delta q}{q}\right) \frac{2R}{a} \tan\theta \qquad (8)$$

where $N_{tot}$ is the total number of pixels of the detector (assumed to be square). With focusing, $I_0$ depends on S(q) and on $\cos^2(2\theta)$ (polarization), but not on d. We note that for fixed q (1 Å$^{-1}$), the dependence of $\beta$ on the adjustable parameters can be written as $\beta \propto \lambda R^2/(da)^2$ (quite accurate for the $\lambda/d^2$ dependence, approximate for the $(R/a)^2$ dependence). All in all (approximation: $\beta << 1$), we get

$$SNR \propto S(q) N_{tot}^{1/4} \sqrt{\left(\frac{\Delta q}{q}\right)} \lambda^{1/2} (a/R)^{3/2} \beta \qquad (9)$$

$$\approx S(q) N_{tot}^{1/4} \sqrt{\left(\frac{\Delta q}{q}\right)} d^{-2} \lambda^{3/2} \sqrt{\left(\frac{R}{a}\right)} H(q, h, \Delta\lambda/\lambda) \qquad (10)$$

where $\lambda^{1/2}$ originates from the $(\tan\theta)^{1/2}\cos^2(2\theta)$ term and H is a function that captures $\beta$'s non-trivial dependence on q, $\Delta\lambda/\lambda$, and h (sample thickness). However, H is a monotonous function of the three parameters (decrease with increasing q, h and $\Delta\lambda/\lambda$). In eq. 10, we note the square-root dependence of R/a and the d$^{-2}$ and $\lambda^{3/2}$ terms. The above result is different from the SAXS result (eqs. 6 and 7) in the sense that the SNR gives no guidance for an optimum working condition (c.f. the condition: $a \approx \lambda R/d$ for SAXS).

In this case, it is more instructive instead to look directly at the boundary conditions, e.g. 1) is there a limit of $\beta$ below which one cannot work as the correlation function becomes un-detectable (as discussed above: baseline issue, systematic errors, etc.), and 2) will the sample heat too much from one SASE pulse?
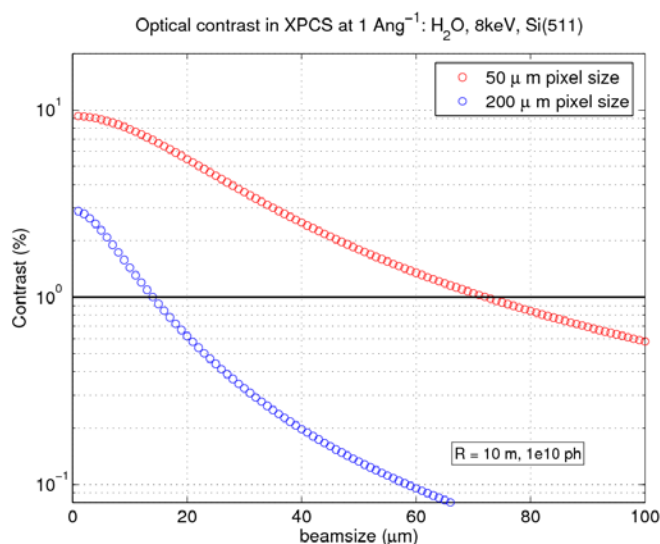
**Figure 12:** *Illustration of the attainable contrast in WAXS XPCS on water with two different pixel sizes. An optical contrast of 1% (solid line) results in a 10 K temperature rise of $H_2O$ for 200 $\mu$m pixels because a 14 $\mu$m beam size must be used. The corresponding value for 50 $\mu$m pixels is only 0.4 K as the beam size can be relaxed to 70 $\mu$m.*

Without focusing, $I_0$ will depend on $d^2$, hence the $d^{-2}$ dependence of $\beta$ disappears in eq. 10, removing an obvious advantage. Because $I_0$ is also larger in the case of focusing by a factor ($I_{0, focusing}/I_{0, no focusing}$), and since the scattered signal will be a limiting factor in Wide Angle (WA) XPCS, we defer the discussion of the no-focusing case. Hence, focusing is assumed and, again, we look at two illustrative examples, $H_2O$ and Cu, this time at q = 1 Å$^{-1}$ (transmission geometry):

Figure 12 shows the optical contrast for $H_2O$ at 8 keV and a bandwidth $\Delta\lambda/\lambda = 1.1 \times 10^{-5}$ corresponding to a Si(511) reflection. This is really the minimum bandwidth for WAXS XPCS, otherwise the contrast is below the detection level in most cases. Two calculations with different pixel sizes are shown in Figure 12. The case for 200 $\mu$m pixel size is particularly difficult where even 1% contrast will lead to a 10 K temperature rise from a single shot of $10^{10}$ photons. The situation does not improve much by reducing the beam size, and 3% is the maximum attainable contrast. In this case, it could become necessary with masked pixels just to get a possibility to measure anything at all (alternatively lowering the photon energy, see Figure 14). The advantage of 50 $\mu$m pixels is obvious with only 0.4 K temperature rise at $\beta$ = 1% and a maximum attainable contrast of almost 10%.
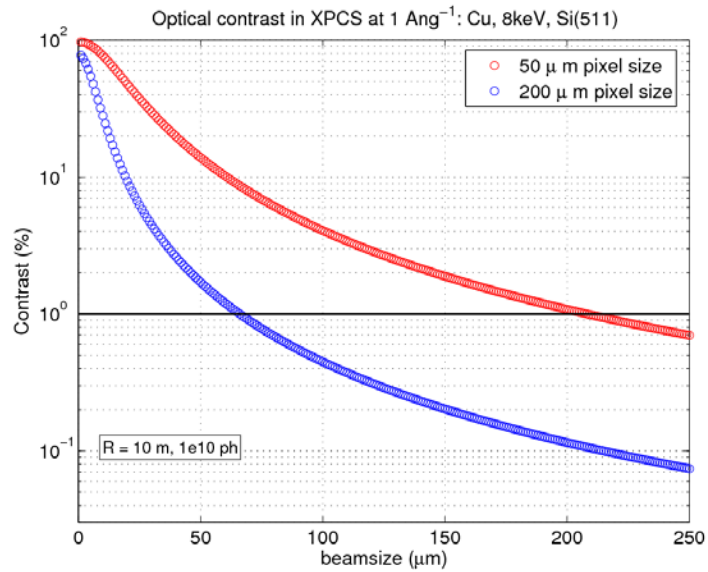
**Figure 13:** *Same as Figure 12 but calculated for Cu. An optical contrast of 1% (solid line) results in a temperature rise of Cu of 24 K for 200 $\mu m$ pixels. The corresponding value is 2.5 K with 50 $\mu m$ pixels.*

The case of Cu shown in Figure 13 is also challenging, but the parameter space is larger, allowing to maximize the contrast by varying the beam size. Certainly, 200 $\mu m$ pixel size complicates the situation, and maybe a higher spectral purity and beam attenuation would be necessary, but pixel masking is not required. The calculations show that a factor of 10 less heat load could be achieved with 50 $\mu m$ pixels

Figure 14 shows the effect of shifting the energy in WA-XPCS assuming a = 200 $\mu m$. Moving to 5 keV is advantageous, not only due to the $\lambda^{1/2}$ factor in eq. 9 but also because it allows obtaining a decent contrast with less heat load, especially important for the $H_2O$ case where the temperature rise for $\beta$ = 1% reduces by almost a factor of 4 going from 8 to 5 keV in photon energy. Hence, in this geometry lowering the photon energy has the same effect as reducing the pixel size and would be a valuable option. For $H_2O$, at 5 keV the maximum achievable contrast is now about 10%, and 5% can be reached with a 10 $\mu m$ beam size. In this case, pixel masking would probably not be needed. The advantage of using 5 keV photons in high-Z materials like Cu is less striking, but it allows getting a slightly better SNR and a slightly smaller $\Delta T$ with larger beams. Figure 14 clearly shows that higher photon energies (24 keV) should be avoided in WA-XPCS: for high-Z materials, the heat load is too big, while for low-Z materials the contrast is too small.
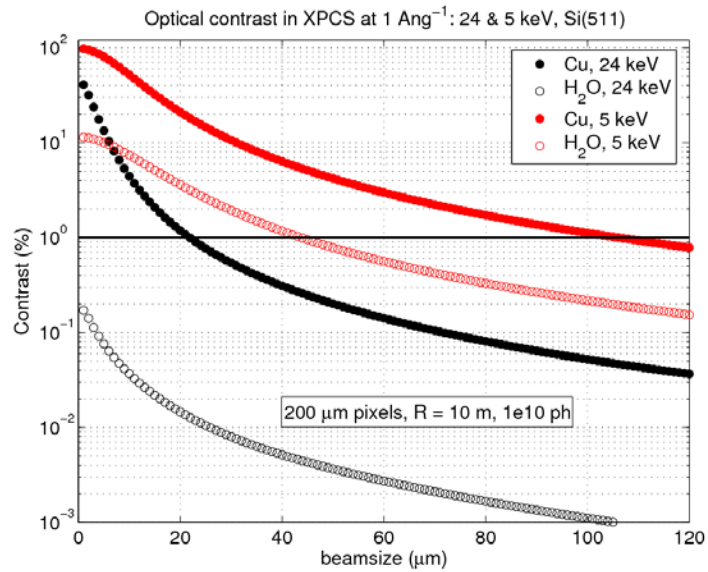
**Figure 14:** *Effect of changing energy for 200 $\mu$m pixel size. For Cu, the temperature rise at 1% contrast is 22 K (5 keV), very similar to the 8 keV case (compare to Figure 13 caption). At 24 keV, the corresponding number is 266 K! For $H_2O$, the temperature rise is 2.7 K at 5 keV, i.e. only about a quarter of the rise using 8 keV photons (compare to Figure 12 caption). At 24 keV, XPCS at q = $1\mathring{A}^{-1}$ is impossible on water in this geometry.*

The outcome of the analysis is summarized in Table 2.

**Table 2:** Summary of the SNR analysis for XPCS

|  | **SAXS regime** | **WAXS regime** |
|---|---|---|
| Low-Z materials | Variable photon energy; BW $10^{-3}$–$10^{-5}$; focusing down to 10 $\mu$m; no detector masking; moderate $\Delta T$; high contrast, good SNR | Lowest energy possible; BW $10^{-5}$; focusing down to 1 $\mu$m; maybe detector masking; $\Delta T$ an issue; low contrast, low SNR |
| High-Z materials | Stay below K-edge; BW $10^{-3}$–$10^{-5}$; focusing down to 10 $\mu$m; no detector masking; huge $\Delta T$; high contrast, good SNR | Stay below K-edge; BW $10^{-5}$; focusing down to 1 $\mu$m; no detector masking; big $\Delta T$; medium contrast, low SNR |

For many WAXS scattering experiments, single photon events will dominate the detector signal and, in general, this situation can be expected when the scattering is weak. In this case, the images can be readily analysed by a droplet algorithm [67] to reduce the effect of charge sharing between adjacent pixels and find the point of impact of the individual photons, even beyond the spatial resolution given by the detector. The intensity correlation function then

reduces to a photon event correlator where the contrast of the correlation functions is less affected by the detector resolution. Typically, one can gain 1–5% compared to the calculations in Figures 12–14, which will have a large impact for certain WAXS experiments where the contrast is low.

Finally, we mention that, since many of the XPCS and imaging experiments at the European XFEL will have a very low photon count rate per pixel, a detector with greatly reduced dynamic range could be used with advantage if it would allow reducing the pixel size beyond the current specifications of AGIPD. Preliminary studies indicate that 100 μm pixel size is within reach if the dynamic range and the detector memory are reduced, but this needs further confirmation, and realization of an AGIPD-type detector with smaller pixels will require additional funds. Also, for certain experiments, the 4.5 MHz repetition rate of the detector is not mandatory, so speed could also be traded for a reduced pixel size, if possible. Other important points are the requirements concerning external background (ideally the detector should be free of background) and detector noise (false hit probability < 1 count per frame) at photon energies as low as 5 keV. At these energies the detector noise contribution is significant in the current design and could render the experiments difficult.

## Ultrafast XPCS

The time structure of the superconducting XFEL linac suggests that the minimum timescale possible in correlation spectroscopy will be 220 ns, which is the spacing between successive pulses within a pulse train. However, this need not to be a hard limit if i) special linac modes with smaller bunch separation will be available (at LCLS, a mode with a few ns separation between bunches was already demonstrated), or ii) a split-delay unit can be used in the photon beam to turn one pulse into two pulses of equal intensity and a time separation (delay) has been introduced by a path length difference between the pulses. In any case, the fastest 2D detector currently planned (operating at max. 4.5 MHz) will not be able to distinguish images originating from the two pulses—it will just record the sum—and a special version of XPCS has to be used.

As the detector records the sum of two images of a certain delay time $\tau$, the contrast $\beta$ of the speckle image will be equal to the nominal optical contrast

only if the two speckle images are perfectly correlated, i.e. if the sample is static on timescales $t < \tau$. If, on the other hand, the two speckle patterns are only partially correlated, the behaviour of the contrast $\beta$ as a function of $\tau$ and q will reveal the characteristic timescales and nature of the dynamics. It is easy to show that, by calculating $\beta(q,\tau)$ in this manner, the same information is available as obtained in the usual intensity–intensity temporal autocorrelation function $g^{(2)}(q,\tau)$. To properly evaluate $\beta$, many double-exposures with fixed $\tau$ will be required. How many depends on the statistics of the patterns. Dispersion relations can be mapped out as the detector covers several q values, and most of the advanced analysis in terms of two-times correlation functions $G(t_1,t_2)$, dynamical susceptibility $\chi$, and even higher-order correlation functions could be calculated.

The contrast of a speckle pattern can be quantified by a visibility analysis, or more precisely by calculating the spatial two-point correlation function

$$g(r_1, r_2) = \langle \frac{\langle I(r_1)I(r_2) \rangle}{\langle I(r_1) \rangle \langle I(r_2) \rangle} \rangle_\phi \qquad (11)$$

where $r_1$ and $r_2$ indicate the position of the two pixels. The averaging over $\phi$ corresponds to an ensemble averaging over the chosen area of the detector, e.g. having a constant q = $|q|$. The contrast is now found by taking the limit $r_1 = r_2$ of $g(r_1,r_2)$ and can be evaluated as

$$\beta = \mathrm{var}(I)/\langle I \rangle^2 \qquad (12)$$

with the usual variance $\mathrm{var}(I) = \langle I^2 \rangle - \langle I \rangle^2$. An alternative method to determine $\beta$ is by analysing the distribution of the intensities of the speckle pattern. It is well known [68] that the Poisson-Gamma distribution describes the probability of finding a pixel with intensity I within a speckle pattern and is given as

$$P_M(I) = M^M \left( \frac{I}{\langle I \rangle} \right)^{M-1} \frac{\exp(-MI/\langle I \rangle)}{\Gamma(M)\langle I \rangle} \qquad (13)$$

where $\beta$ = 1/M and $\Gamma$ is the usual Gamma function. $P_M(I)$ is shown in Figure 15 for different values of $\beta$. For a quick evaluation of $\beta$, it is interesting to focus on the most probable intensity or alternatively on the probability of detecting zero photons in a pixel. Both these quantities are sensitive to $\beta$, as

shown in detail in Figure 16. Alternatively, the FWHM of the distribution or the standard deviation $\sigma = \langle I \rangle / \sqrt{M}$ can be used to track the contrast. In this way, XPCS at ultrafast timescales is within reach, in principle only determined by the minimum delay that can be introduced by a delay line or directly in the accelerator. With the current performance of photon split-delay lines, it should be possible to generate delays up to a few ns. The possibility to close the gap up to 220 ns relies on modifying the linac pattern in parts of a train, but this should, in principle, also be feasible.

Importantly, in the ultrafast XPCS scheme outlined above, the timescales on which the dynamics can be probed are not directly linked to the speed of the detector. Hence, this mode offers the possibility to use a slower detector operating at 10 Hz or in the kHz range (e.g. a CCD or a commercially available pixel detector), which then could have much smaller pixels. Detection with small pixels brings the experiment into a high-contrast mode where the SNR can be optimized taking sample damage and other effects into account.
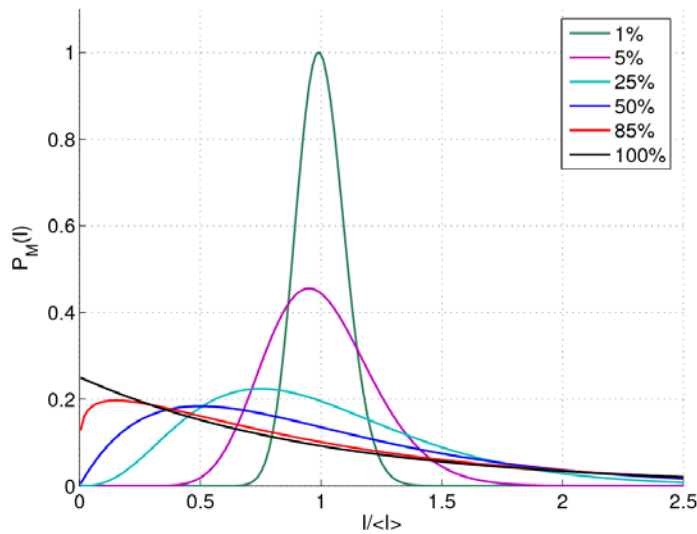


**Figure 15:** *Poisson-Gamma distribution (eq. 13) for different values of $\beta$*
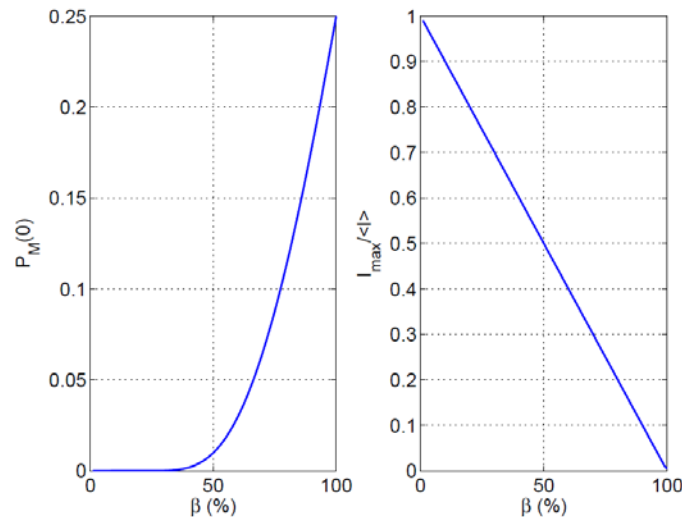
*Figure 16:* *Probability of finding pixels with zero intensity, $P_M(0)$, and the normalized value of the most probable intensity value in a pixel ($I_{max}/<I>$) vs. $\beta$. For low-contrast values, $I_{max}/<I>$ is the most sensitive measure. A salient feature of high-contrast speckle patterns is that 0 in the most probable intensity.*

# Feasibility of CXDI

For Coherent X-ray Diffractive Imaging (CXDI) experiments, the figure of merit is the resolution obtained in the reconstructed images of the sample. Clearly, for the single molecule imaging taking place at the SPB instrument, the goal is to achieve atomic resolution and be competitive with usual crystallographic methods. For the CXDI experiments at the MID station, the goal is to image nano- to micron-sized objects in a non-destructive manner that also allows 3D resolution. This puts the efforts in direct competition with storage-ring-based synchrotron radiation (SR) experiments, but the approach to design an experiment will be different. For SR CXDI, the paramount challenge is the limited coherent flux and problems related to missing data close to the direct beam. This makes the experiments very challenging as it requires the beamline and sample to be stable over hours of acquisition time. For materials science CXDI experiments at the MID station, the major challenges will be to handle the radiation damage problem and have a detector that fulfils the special requirements. For both SR and XFEL CXDI, a

measured wavefront profile is also important as input to the reconstruction algorithms.

The detector size and resolution is, as for XPCS, one of the most important parameters. In CXDI, the speckle images need to be correctly sampled according to the Nyquist-Shannon theorem and so

$$q_{res} \leq q_{speckle}/2 \tag{14}$$

where $q_{res}$ is the q-resolution of the detector set by the pixel size (a), the sample–detector distance (R), and the wavelength $\lambda$. The reciprocal speckle size $q_{speckle}$ is roughly given by $2\pi/r$ where r is the size of the sample. Hence we get

$$\frac{a}{R} \leq \frac{\lambda}{2r} \tag{15}$$

or

$$R = \frac{2\Omega a r}{\lambda} \tag{16}$$

where $\Omega > 1$ is the degree of over-sampling. The best real-space resolution $\delta r$ that can be obtained in CXDI is like in diffraction, i.e. determined by the maximum scattering vector that can be measured like $\delta r = 2\pi/q_{max}$. Assuming the detector to be centred on the direct beam, in the small-angle approximation $q_{max}$ is given by $q_{max} = \pi N a/(\lambda R)$, and we find the limit for the relative resolution

$$\frac{\delta r}{r} = \frac{2\Omega}{N}. \tag{17}$$

Hence, in an ideal world ($\Omega = 1$) with a detector of N $\times$ N pixels (N ~ 1 000), we could expect the best resolution to be 1/500. This depends only on the over-sampling ratio and on the number of pixels. The over-sampling condition, eq. (14), needs to be fulfilled and, typically, one works with $\Omega \approx 2.5$–5 in 2D CXDI, meaning that the area covered by a speckle is 5–10 times larger than $a^2$. Higher over-sampling ratios can lead to a better convergence of the iterative phase-retrieval algorithms and give better noise tolerances. In addition, more missing speckles can be tolerated (removable artefacts) if the over-sampling ratio is large, hence yielding a tendency to

work at $\Omega = 5$ and only 100 resolution elements. In this case, up to about 13 missing speckles (130 pixels) can be tolerated without influencing the result. The threshold for removable artefacts seems to be around 300 missing pixels [69].

We take a CXDI experiment on a 3 μm cell (low-Z material) as an illustrative example. Here, we only consider forward scattering (SAXS) since the Bragg case on high-Z materials will be less critical. For a 3 μm diameter near-spherical cell, the speckle size (area) is approximately $2 \times 10^{-4}$ Å$^{-2}$. Using the equations above, it is easy to see that the 1D over-sampling ratio for 5 keV radiation (a = 200 μm and R = 10 m) is 2, or 4 in 2D. Such an over-sampling ratio is possible in real experiments with missing central intensities and noise dominated data at high q. In this case, it is estimated that $10 \times 10$ central pixels can be missing without any problems for the reconstruction. It is proposed to focus the beam on the detector in order to have as little missing data at possible and fit in 100 central pixels, or preferably less. This should be an easy condition to fulfil. This "dead area" could be realized either by using a lead or a tungsten mask, or via a real hole as for the CXI detector at LCLS, but it must be adjustable as its maximum acceptable size gets smaller if the oversampling ratio is decreased.

For the thermal load calculations, we approximate the cell by 3 μm water droplet with a weight of about 15 pg. Assuming $10^7$ photons hitting the sample per shot, we find at 5 keV (1% absorption) that the sample heats by 1.3 K. The corresponding number for 10 keV is a 10 times smaller absorption but a temperature rise that is only 4 times smaller. Hence, if there are no other constraints, this means that low-E operation is favoured, similarly to the XPCS requirements in WAXS geometry on low-Z samples.

Simulations of a scattering pattern from a model cell are shown in Figure 17. Clearly, a detector with single photon sensitivity is required to record such patterns on the single-shot level when the temperature rise has to be minimized. This favours low energy operation, which again sets requirements to the detector performance, similarly to the XPCS discussion above. However, assuming single photon sensitivity of the detector, the simulations indicate that CXDI is possible in this mode and multiple exposures can be envisaged. Pursuing this technique would ideally require a spherical detector

with as many small pixels as possible and single photon sensitivity at 5 keV. In this case, the detector speed is less significant.
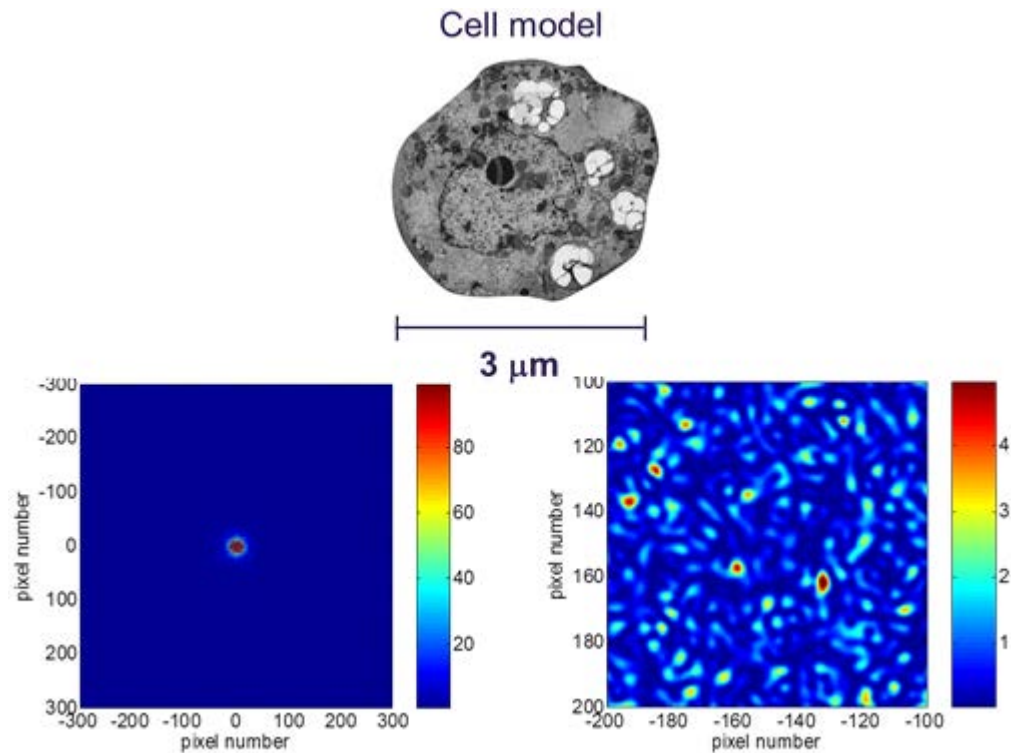


*Figure 17: Simulation of a CXDI experiment from a model cell as described in the text. The right image is a zoom on a region of the left image illustrating the few counts expected. A few photons per pixel is the maximum intensity, except very close to the direct beam.*

The multi-exposure mode is, in particular, interesting if the intrinsic time resolution of the European XFEL is exploited for CXDI *in situ* studies or in tomographic 3D or ptychography experiments. Similarly to the ultrafast XPCS case discussed above, if the full time resolution (i.e. 4.5 MHz) is not needed, employing a slower detector featuring either more or smaller pixels (or both) could be envisaged. For CXDI, it seems more difficult to relax on the detector specifications concerning the dynamic range as large intensity variations within a single frame can be expected both in forward and Bragg scattering geometries.

The detector requirements for XPCS and CXDI are summarized in Table 3.

**Table 3:** *Summary of detector requirements for XPCS and CXDI*

| Applications | Detectors | | |
|---|---|---|---|
| | **Spatial resolution requirements** | **Features in addition to AGIPD specifications** | **Comments** |
| High-energy scattering experiments | | High energy sensitivity (must) | |
| Small-angle XPCS (sequential mode) | Spatial resolution ~ 100 $\mu$m (recommended) < 50 $\mu$m (advantage) < 25 $\mu$m (optional) | | 4.5 MHz speed must be kept. Maybe smaller dynamic range or less memory required |
| Wide-angle XPCS (sequential mode) | Spatial resolution ~ 50 $\mu$m (recommended) < 25 $\mu$m (advantage) | Higher sensitivity and lower noise at 5 keV (must) | 4.5 MHz speed must be kept. Reduced dynamic range possible |
| Split-delay XPCS | Spatial resolution ~ 50 $\mu$m (recommended) < 25 $\mu$m (advantage) | | Need not to operate at 4,5 MHz |
| Coherent X-ray Diffractive Imaging | Spatial resolution ~ 100 $\mu$m (advantage) < 50 $\mu$m (optional) | Higher sensitivity and lower noise at 5 keV (must). As many pixels as possible | Curved surface covering half sphere (optional). Maybe not 4,5 MHz operation |

# MID station: conceptual design

This chapter describes the conceptual design of the MID instrument reflecting the close interplay between the instrumentation, the science and experiments at target, and the requirements to beam characteristics, optics, and detectors that are inextricably linked.

## Introduction

It is considered of highest priority that the instrument can operate in an optimized mode covering the SASE energy range from 5 to 25 keV with a variable beam size from 1 to 200 $\mu$m. Photon energies higher than 25 keV are also interesting, and even the spontaneous hard X-ray regime (50–200 keV) or higher (up to 1 MeV) could be attractive for certain experiments, as described in the previous chapter. Simulations suggest that, for photon energies higher than ~ 40–50 keV, the spontaneous radiation from the undulator will be stronger than the higher-order SASE harmonics. As described in the previous chapter, this hard end of the spectrum is also more brilliant than at any synchrotron source and hence will be attractive to exploit. The SASE2 undulator delivers photons down to 3 keV, but optimized experiments in the range 3–5 keV require the use of reflective Kirkpatrick-Baez (KB) or diffractive Fresnel Zone Plates (FZP) as focusing optics instead of the Beryllium Compound Refractive Lenses (CRL) that are foreseen at the MID station to cover the range from 5 keV and above. While FZPs in principle can replace CRLs without too much trouble, the requirements to cooling and damage thresholds are quite different. Also, restrictions in the use of windows and the vacuum requirements hamper the exploitation of photons with energies lower than about 5 keV. Hence, we refrain from further discussion of the 3–5 keV possibility here.

To achieve an energy bandwidth better than $10^{-3}$, as needed for certain experiments, a seeding scheme (e.g. the elegant self-seeding scheme using a wake monochromator proposed by Geloni et al. [70]) is preferred; however,

it is still awaiting to be validated experimentally. As detailed in preceding chapters, the pixel size of 2D imaging detectors similar to the AGIPD detector imposes a bandwidth of $10^{-5}$ for XPCS in WAXS geometry, and it is proposed to install monochromators—a Si(111) pre-mono and a Si(511) high-resolution mono—as close to the experimental setup as possible. The monochromators will benefit from a large distance to the source due to the natural divergence (~ 1 $\mu$rad) of the beam [71], so this is the optimum position to minimize heat load effects that otherwise will severely limit the throughput of the first monochromator [71]. Considering vibration and stability issues, a setup with two monochromators is preferred over a scheme with just one high-resolution mono going directly to $10^{-5}$ BW. Focusing of the beam can then take place only after the monochromators. Obviously, if the self-seeding scheme described above proves efficient and reliable, these monochromators can be left out for many experiments and/or used in a later stage with different crystals if resolution beyond $10^{-5}$ is required.

Options for creating delays up to 220 ns must be investigated in detail. Delay lines based on perfect crystals or grazing incidence mirrors can produce delays in the fs-to-few-ns range. Delays from a few ns to 220 ns are preferably created in the linac by custom filling patterns, and some flexibility exists in putting pulses closer together than the canonical 220 ns. In principle, the range from about 800 ps to 220 ns could be covered [72]. The $\mu$s range, up to 600 $\mu$s (train length), can be accessed in multi-exposure mode by acquiring frames within the same pulse train. In spilt-delay mode, the detector speed is not determining the time resolution of the experiment but only the duty cycle.

The 4.5 MHz operation of the AGIPD detector is mandatory to capitalize on the high average brilliance and time structure of the European XFEL and is essential for sequential XPCS. As demonstrated in the previous chapter, however, 200 $\mu$m pixel size requires a combination of focusing, small bandwidth, beam attenuation, and low photon energy (5 keV) operation for many WA XPCS experiments to within reasonable feasibility limits. These conditions define one limit of the experimental conditions the MID station must be able to deliver in order to study e.g. the bulk metallic glass dynamics as described in "Glassy dynamics" on page 13. The other limit is illustrated by

the single-shot X-ray holography/CXDI experiments described in "Biological imaging" on page 23, where the pink beam obviously can be used.

# Conceptual design details

### Beam transport and optics

Due to their simplicity and robustness, it is proposed to use compound refractive lenses (CRL) for focusing the beam down to the required size. CRLs are refractive lenses made in a low-Z material, commonly Be, and have the right concave parabolic shape ($x^2/r$) which is required for a focusing lens. The focal length f of a CRL assembly is
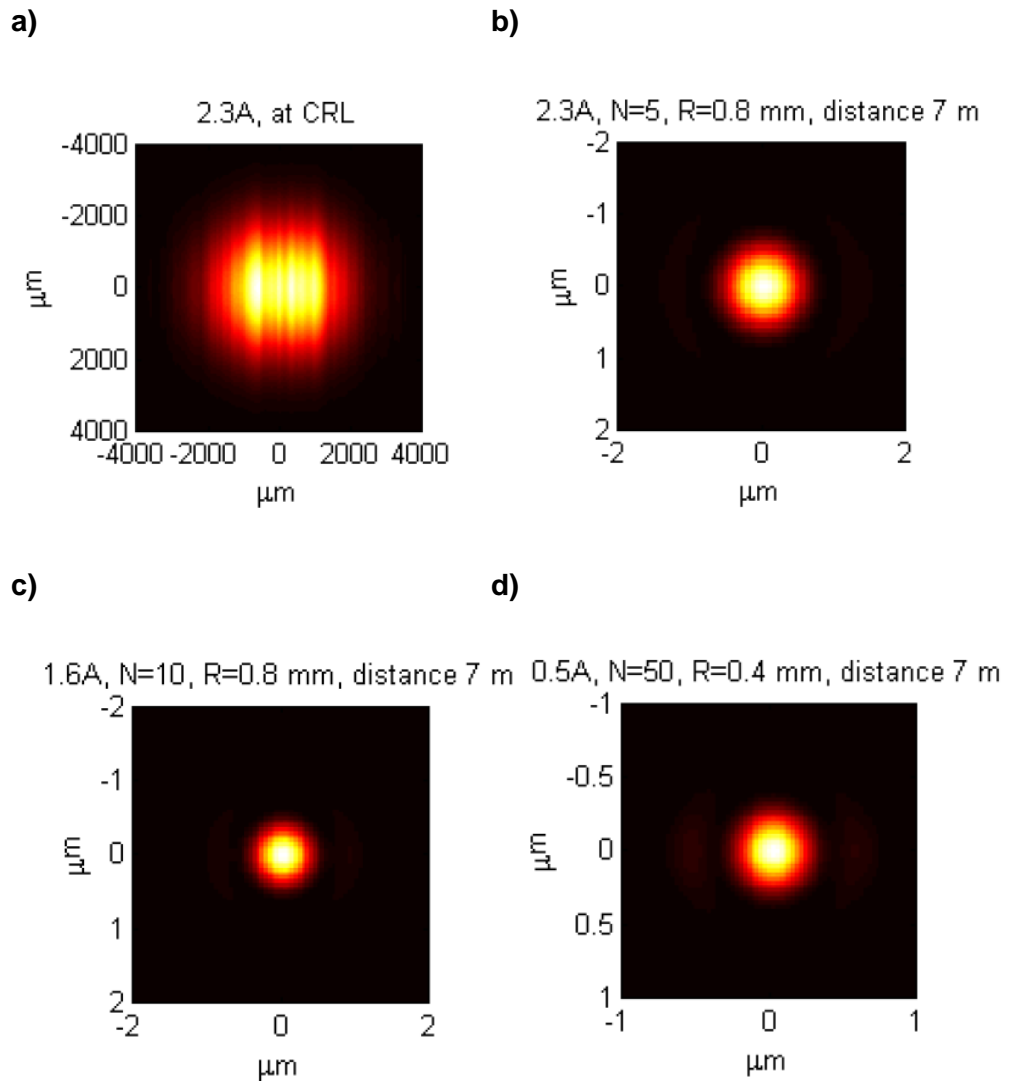
$$f = \frac{r}{2N\delta}. \qquad (18)$$

where r is the radius of curvature of the parabola, N is the number of lenses, and 1-$\delta$ is the refractive index of the material. The lens acceptance is approximately 2.5 times r, hence, if a 0.5 mm beam (FWHM) is the required acceptance, one finds r = 0.2 mm. For Beryllium we have $\delta \sim \lambda^2$ [$\text{Å}^2$] $\cdot$ 2.2 $\times$ $10^{-6}$, and hence the focal length of one lens with r = 0.2 mm is ~ 19 m at 8 keV. The proposed optical scheme (see Figures 19–21) employs a CRL assembly after the monochromators in the optics hutch to focus the beam. A varying number of lenses must be inserted, depending on the photon energy and the beam size wanted. It is envisaged to be able to focus both at the sample and the detector position, and to operate with the sample out of focus to increase the beam size, thereby decreasing the heat load. For CXDI, it is an advantage to place the sample in the focal point since the beam is very well defined and clean, as shown in Figure 18. Table 4 lists examples of the parameter space covered by a multi-lens CRL assembly placed 960 m from the source and 7 m upstream of the sample. The number of lenses (N) and the acceptance (~ 2.5 $\cdot$ r, depending on the absorption) is given together with the photon energy for focusing at the sample position. Also shown is the energy range over which the beam size (FWHM) on the sample is smaller than 200 $\mu$m. Some of the proposed lens assemblies can also be employed to focus the beam on the detector (assumed 10 m downstream from the sample) as indicated.

The theoretical minimum focal spot on the sample is around 0.3 μm, but, due to lens imperfections and illumination with a divergent and non-perfect wavefront (from the offset mirrors, see Figure 18), we expect this lower limit to be rather 1–2 μm, depending on the energy. This is confirmed in the simulations in Figure 18, which also demonstrates how focusing can clean up a disturbed wavefront.

*Table 4: Summary of the proposed CRL arrangement in the optics hutch 960 m from the source and 7 m from the sample*

| Number of lenses (N) | Acceptance (mm) | Focus on sample (keV) | E range (keV) | Focus on detector (keV) |
|---|---|---|---|---|
| 3 | 3 | – | – | 5.3 |
| 6 | 3 | 4.9 | 4.7 – 5.0 | 7.5 |
| 5 | 2 | 5.5 | 5.2 – 5.7 | 8.4 |
| 10 | 2 | 7.7 | 7.3 – 8.1 | – |
| 17 | 2 | 10.0 | 9.5 – 10.5 | – |
| 18 | 1 | 14.5 | 13.3 – 16.2 | – |
| 34 | 1 | 20.0 | 18.3 – 22.3 | – |
| 50 | 1 | 24.4 | 22.1 – 26.3 | – |

A second CRL multi-lens assembly situated at the end of the tunnel 930 m from the source could allow obtaining an even wider flexibility in choosing energy, beam size, and focal position (on the sample or on the detector). Great care, however, must be taken in operating this device, together with the downstream monochromators, as the crystals will be damaged if they are close to or in the focal spot. This is also true for the third CRL unit, placed 230 m from the source to make the beam parallel, which cannot be operated together with the monochromators without beam attenuation [71]. Slit units upstream of the CRL units will allow collimation of the beam impinging on the lenses. This ensures that the flux on the sample can be varied in a continuous way by adjustment of the slit apertures. Alternatively, the beam size and flux may be varied by a combination of attenuation and focusing. Small beam sizes are typically needed for WA-XPCS, while larger beams can be tolerated and even desirable for certain SA-XPCS and CXDI experiments.

a)

2.3A, at CRL



b)

2.3A, N=5, R=0.8 mm, distance 7 m



c)

1.6A, N=10, R=0.8 mm, distance 7 m



d)

0.5A, N=50, R=0.4 mm, distance 7 m



*Figure 18: a) Simulation of the SASE intensity distribution at 5.5 keV, right before the CRL at 960 m from the source. The striped pattern originates from coherent illumination of the two offset mirrors. b), c), and d) Intensity distribution at the sample position 7 m downstream for 5.5, 7.7, and 24.4 keV, respectively. This corresponds to three different CRL configurations from Table 4. Wavefront simulations courtesy of L. Samoylova, European XFEL.*

It is proposed to install two monochromators employing Si(111) and Si(511) reflections (pre- and high-resolution) in an optics hutch just before the experiment. This gives the possibility to work at a bandwidth of either $10^{-4}$ or $10^{-5}$. The monos should be channel-cut types diffracting in the vertical plane [71]. The beam offset is $d \cdot \sin(2\theta)/\sin(\theta)$, where $\theta$ is the Bragg angle, yielding less than 10% changes in the vertical position of the outgoing beam as the energy is scanned from 5 to 25 keV for Si(111). Hence, for a crystal separation of $d = 10$ mm, the deviation from a mean beam offset  is less than

2 mm over the entire energy range, which is an acceptable requirement to adjustments and apertures of the downstream beamline components. If the high-resolution mono is used together with the pre-mono, it may actually compensate the vertical offset and bring the beam back toward the optical axis.

The monochromator crystals should be removable either if the pink beam is required in the experiment hutch, if the diamond Laue double crystal monochromator is inserted upstream, or if the seeding scheme mentioned above proves to be a reliable alternative. Details about the monochromators planned for the European XFEL are detailed in the beam transport and optics CDR [71]. We stress that placing the two channel-cuts as far away from the source as possible is essential for minimizing the heat load and hence maximizing the number of pulses out of a pulse train that will be delivered to the experiment. A cryo-cooled channel-cut Si(111) monochromator at this position will transmit about 1 000 pulses/train in the 5–25 keV range [71], which actually exceeds the storage capacity of the currently planned AGIPD detector.

XPCS and CXDI experiments are very sensitive to beam instabilities and fluctuations, so it is proposed to locate the MID experiment as close as possible to the monochromators. For reasons of coherence preservation and energy range and tunability, the MID station occupies the central branch of SASE2 (no distribution mirror, see Figure 19), so if placed upstream in the SASE2 experiment area, two beam pipes (one on each side of the instrument separated by 2.8 m, see Figure 19) would surround the instrument. This is a challenging arrangement, preventing the operation of a diffractometer and the long horizontal detector arm (see Figure 23). Hence, it is proposed to locate MID downstream of the HED station (side branch) towards the end of the SASE2 area (see Figure 22).[5]

Other than the offset-mirrors in the optics hutch, smaller local mirrors are required closer to the sample to be able to direct the beam downwards (for grazing incidence studies on liquids) and to clean up the harmonic content

---

[5] In a detailed surface plan of the various instruments and hutches, the HED requirements must of course be taken into account.

from higher-order monochromator reflections. Local mirrors made of Si can be employed up to about 25 keV, at higher energies the beam is preferably tilted down by use of single crystal reflections.

A Laue double crystal monochromator is required to monochromatize beams with energies higher than about 25 keV and direct them around the main beam stop. Diamond DCM schemes are in use at several hard X-ray synchrotron stations around the world and the crystals can be bent to increase the energy acceptance if necessary. Details about the Laue diamond DCM design will need to be decided later, and we propose to undertake a detailed simulation study of its performance. A pre-study of the performance of a cryo-cooled diamond DCM at high photon energies was undertaken [71], concluding that oscillations in transmission due to the Pendellösung effect become negligible as the photon energy increases. The study indicates that such a monochromator indeed could be conveniently operated yielding a relatively high throughput up to about 200 keV. If the SASE lines can be suppressed in this special operation mode, the Laue DCM could also be based on Si crystals.

Both a perfect crystal–based split-delay line and a grazing incidence mirror–based split-delay line will be needed for the experiments as discussed previously. The grazing incidence split-delay line (auto-correlator, similar to the device operating at FLASH) will be build by Prof. Zacharias' group at the University of Münster and made available to the European XFEL. According to the current specifications, this device will be able to produce fs–ps delays over a range of hard X-ray energies. It is proposed to place this split-delay line unit in the tunnel. As it is cooled and operates under grazing incidence conditions, the load of the full beam can be accepted at this location. The Bragg crystal–based split-delay line operates at discrete energies; it is not cooled and requires that the beam is pre-monochromatized in order to remove heat. Therefore, this device should be placed in the optics hutch after the two monochromators. The Bragg delay line will cover the 10 ps – 3 ns range, where the grazing incidence delay line cannot operate.

Slit units and attenuator boxes, as well as positioning and diagnostics tools (YAG screens, cameras, diodes, foil detectors), will be needed at strategic places along the beam path starting from right after the SASE undulator until the beam reaches the experiment station and hits the sample. For certain

samples and experiments, the incident intensity can be measured after the sample in transmission geometry. Particularly challenging will be the integration of X-ray transparent intensity and position monitors able to provide single pulse information with high precision over a wide range of X-ray energies. Gas filled ion chambers are currently being developed for this purpose, both for absolute and relative intensity measurements. A precise timing diagnostics is also required to measure and control the jitter in optical pump – X-ray probe measurements. Sketches of the SASE2 beamline in the XTD6 photon tunnel and the MID specific tunnel optics are shown in Figures 19 and 20.
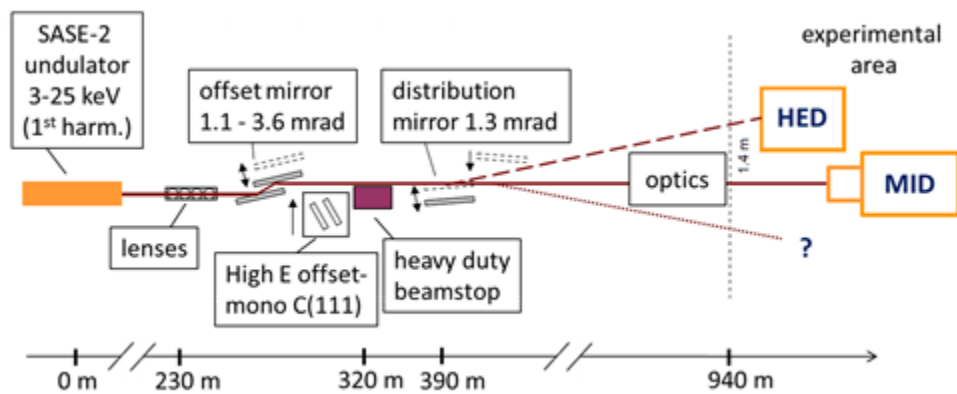


**Figure 19:** *Sketch of the beam path in the XTD6 photon tunnel from the SASE2 undulator to the experiment area. The high E C(111) offset mono (~ 315 m from the source) and the optics section (~ 915 – 940 m, see Figure 20) are specific to the MID station, which will be located towards the end of the SASE2 experiment area (see Figure 22). Figure adapted from ref. [71].*
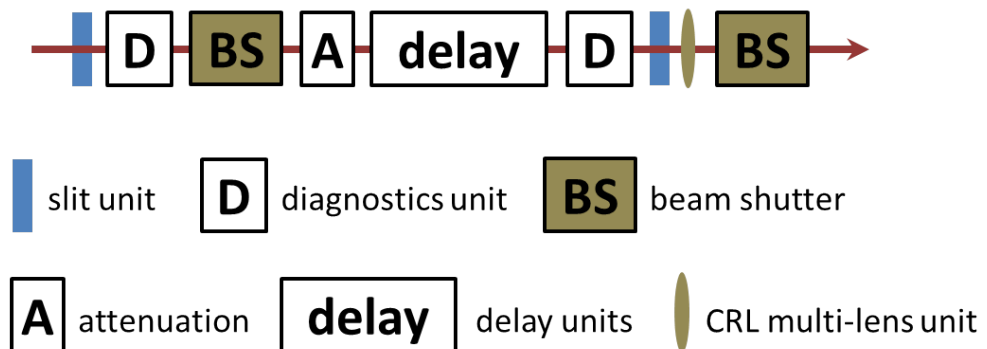


**Figure 20:** *Schematics of the approximately 15 m long optics section specific to the MID station located at the end of the XTD6 photon tunnel. The grazing incidence spit-delay unit itself is about 7 m long. The optics is placed ~ 930 m from the source, just before the beam enters the SASE2 experiment area (see Figure 19).*

A few additional comments can be added to Figure 19 and the proposed tunnel optics arrangement sketched in Figure 20. First of all, it is desirable to install a diagnostic unit (not shown) closely after the undulator exit, which necessarily must be accessible by all the stations at the SASE2 beamline. (The MID, HED, and a third station will be defined and build later. The stations will not operate in parallel, at least initially, so no alignment conflicts are foreseen.) In addition, the offset mirrors and the high-energy Laue monochromator will need their proper alignment tools, including diagnostics and slits, which are also not shown in Figure 19. It is proposed to operate diagnostics units that provide access to beam intensity and position, ultimately on the level of a single shot, but also using low-tech solutions, like video images of fluorescent screens that can be inserted in the beam (similar to the LCLS solution for a generic diagnostic unit for the hard X-ray beamlines). Importantly, the sensitivity of the diagnostics must be adapted to the beam conditions at the location (white beam, monochromatic beam, attenuated beam). As seen in Figures 20 and 21, it is envisaged to surround every optic unit by diagnostics tools and a number of slits are also required to tailor the beam.

As discussed above, the monochromators need to be located close to the MID experiment hutch, which, in turn, is pushed towards the end of the experiment area to avoid conflicts with the side branches. This necessitates an optics hutch placed about 960 m from the source in the middle of the SASE2 experiment area. This optics host the two monochromators, the Bragg split-delay line, and the CRL unit described in Table 4. An outline of the optical components in the optics hutch is shown in Figure 21.

**Figure 21:** *Optical components in the MID optics hutch. It is estimated that at least 7 m is needed to accommodate all the elements. The delay line unit employed here is of the Bragg type. The CRL multi-lens configuration allows to adjust the beam size on the sample (located 7 m downstream) as indicated in Table 4.*

The two monochromators in the optics hutch are of the pseudo channel-cut type (non-monolithic) inspired by the APS design [71]. It is proposed to operate with Si(111) (mono1) and Si(511) (mono2), and, at the European XFEL, due to the high average flux within a train, such devices need to be liquid nitrogen cooled and placed as far away from the source as possible in order to transmit a maximum number of pulses within a train [71]. Possibly, water cooling will be sufficient for the high-resolution mono2.

The slit units upstream of the CRLs are used to limit the illuminated lens area, hence controlling the intensity in the focal spot. The beam shutters (see Figures 20 and 21) are placed according to the two limiting cases of operation also known from synchrotrons: Either a continuous illumination of the optical components is desirable for reasons of stability, or unnecessary illumination of the optics need to be avoided for reasons of radiation damage. In the first case, a succeeding beam shutter allows stopping the beam at the exit of the optics hutch and access to downstream areas is possible while keeping the optics "hot". In the latter case, beam shutters/absorbers are placed along to beam path to satisfy all needs (see Figures 20 and 21). An attenuation unit (e.g. based on polished and cooled single crystal diamond) allows tweaking the beam intensity. Even when the first beam shutter in Figure 20 is closed, it is still possible to monitor the beam by the upstream diagnostics module.

# MID experiment hutch

The experiment area available to the SASE2 stations is outlined in Figure 22 together with a possible location of the MID hutches. Figure 22 is a draft sketch, but it takes the as-of-today defined space requirements for laser hutches and electrical cabins accurately into account. A bit of extra space may become available if a proposed shift of the laser hutch into the surrounding escape ways (not shown) proves feasible. Owing to the distance needed to properly resolve speckles for CXDI and XPCS, the MID experiment hutch needs to be relative large, as shown in Figures 22 and 23.
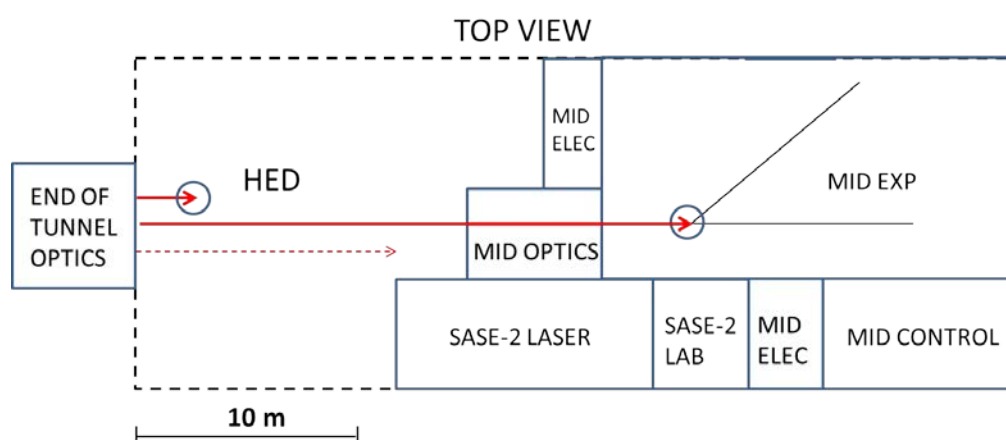


*Figure 22:* *Top view of the SASE2 experiment area (15 x 40 m) starting about 940 m from the source. The MID experiment hutch, electrical hutches, and control cabin, as well as a common SASE2 lab and the laser lab, are indicated. The size of the experiment hutch is determined by the need for 10 m sample–detector distance and hence a 2θ arm of this length capable of moving to 2θ > 45° as indicated on the sketch. The proposed floor layout needs to be reiterated when the requirements of the HED instrument become better defined.*

The 2θ arm is 10 m long, which is the value used in the simulations in the previous chapter concerning the technical details. This arm must be adjustable in height (about 10 mm) because the vertical beam position changes depending on the monochromator(s) in use (if any) and the photon energy. The arm will carry a vacuum flight tube with a detector situated at the end and designed so a 2D detector can be interfaced to the arm.

TOP VIEW

10 m long telescope detector arm

SASE-2

PUMP LASER
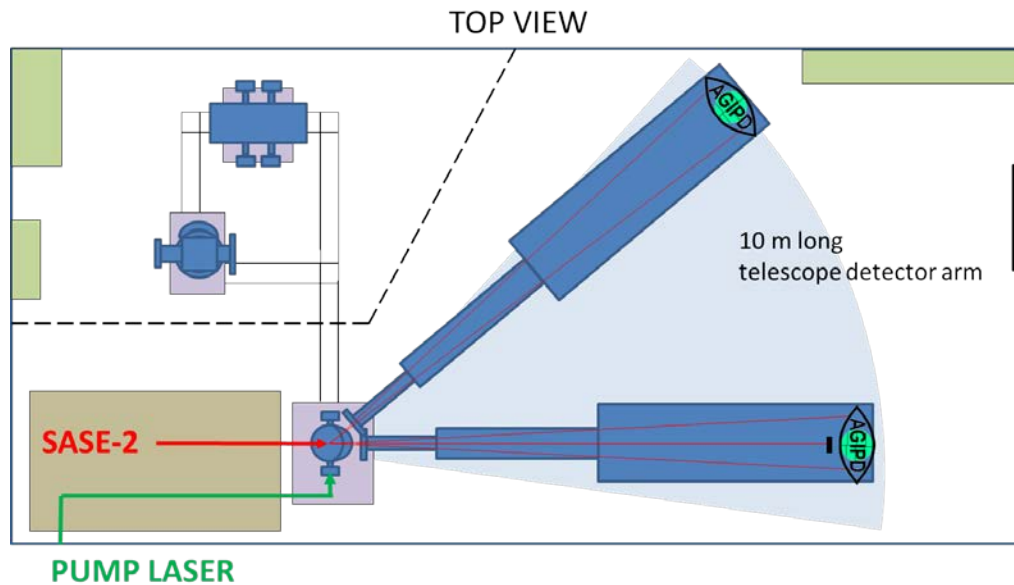
*Figure 23: Top view of the MID experiment hutch (approximately 9 x 18 m) starting about 962 m from the source. The size is determined by the need for 10 m sample–detector distance and hence a 2θ arm of this length, as illustrated. An optics table with mirrors, attenuators, slits, and diagnostics to guide the X-rays and laser beams to a common point of interaction is needed in the hutch. A flexible and exchangeable sample environment is foreseen.*

The optical table indicated in Figure 23 will carry X-ray optics, laser optics, and diagnostics. It is foreseen to operate an optical pump laser up to 4.5 MHz for pump-probe XPCS experiments. The laser beam must be synchronized to the machine and is prepared in an adjacent laser hutch, which is shared by all the SASE2 instruments (see Figure 22). This laser hutch is larger than shown in the SASE2 sketch because it also occupies space outside the SASE2 area. Two X-ray mirrors reflecting in the vertical plane will also be situated at the optical table. They are used to stir the beam downwards for grazing incidence studies on liquid surfaces. In addition, they can be used to remove higher order harmonic content, if required.

For diffraction studies it is proposed to have a four-circle diffractometer with vertical scattering possibilities. This will be achieved via a shorter flight tube (~2 m) carried by the diffractometer's 2θ arm and properly counterweighted for maximum precision. The diffractometer will feature a full goniometer as well as a flexible height adjustment. Sample environments up to about 200 kg must be foreseen. Possibly a commercially available 400 mm Huber diffractometer could be implemented and fulfil the requirements. It is desirable

that the diffractometer also can be operated together with the long horizontal arm. For easy removal and manipulation the diffractometer will be capable of moving on rails installed on the hutch floor. This facilitates a fast switch of sample environments if desired. This idea reflects the MID philosophy of an experiment station aiming at covering a broad range of experiments and an easy change of beam parameters and sample environments.

In addition to the diffractometer necessary for certain WAXS experiment, it is proposed to build a SAXS-compatible sample environment that combines most of the features needed in terms of sample containers (cuvettes, capillaries, flow experiments), sample conditioning (temperature control, B-field), and sample positioning (y-z scanning stages, height positioning) in typical SAXS experiments. A wealth of other customized sample environments can be foreseen, e.g. operating with jets, but for the baseline MID design only the diffractometer and the SAXS setup mentioned above are included. A windowless design is preferred, whenever possible, at least to interface the experimental chamber to the beamline vacuum. This necessitates differential pumping sections for which space needs to be reserved.

A tuneable pump laser operating with fs pulses at 4.5 MHz is considered to be part of the baseline instrumentation as many experiments will be utilizing the short pulses of the XFEL to obtain fs–ps resolution in pump-probe experiments combined with coherent illumination and CXDI/XPCS. This would be the case e.g. in studies of ultrafast demagnetization or other spin phenomena where the dynamics can be triggered by an optical pulse. Proper timing diagnostics and synchronization of the laser and X-ray beams is obviously very critical in pump-probe type experiments if fs time resolution is the aim. Defining the specs and the delivery of a tuneable optical pump laser system to the MID station is a shared task between the MID group and the optical laser group at XFEL.EU.

The detector issue has already been discussed in the "Technical considerations" chapter. It is foreseen that an AGIPD detector with 1k x 1k pixels each of 200 x 200 $\mu m^2$ size will be available in 2015 when first photons become available. The current design of the MID instrument aims at using this detector for as many of its experiments as possible. However, the need for more pixels of a smaller size, and a broader working range of energy, is

obvious. It is unlikely that one 2D detector can satisfy all needs in the future so it is highly recommended to launch a novel R&D project to complement the AGIPD specifications. It is also possible that commercially available CCDs or pixel detectors can satisfy some of the needs in the near future.

# Data acquisition, management, and analysis

The MID station's data acquisition (DAQ), data management (DM), and scientific computing (SC) system architecture foresees multiple levels and will be fully integrated with the hardware and software architecture framework being developed by the XFEL.EU DAQ/DM/SC group for use with all instruments at XFEL. A layered architecture with well-defined interfaces increases implementation flexibility as layers can be introduced, upgraded or removed as required. The architecture design anticipates partitioning all layers associated with single or groups of detectors into separate slices for control, readout and processing purposes.

Six layers are currently foreseen (see Figure 24):

- Front-end electronics (FEE) controls and captures data acquired from the detector head.

- Front-end interface (FEI) interfaces detector FEEs to the timing, control, and readout systems and interfaces to beamline control systems, such as motors, screen cameras, etc.

- PC Layer receives data from detector head FEIs, performs data quality monitoring, formatting and addition processing.

- Online Storage layer provides on-site storage for data acquired and serves data for fast processing before committing good quality data to the permanent archive.

- Offline Storage layer provides both fast and secure storage for data and is planned to be located on DESY site.

- Offline Analysis Clusters (OACs) are used for bulk data analysis of user data, i.e. the Scientific Computing (SC) facility.
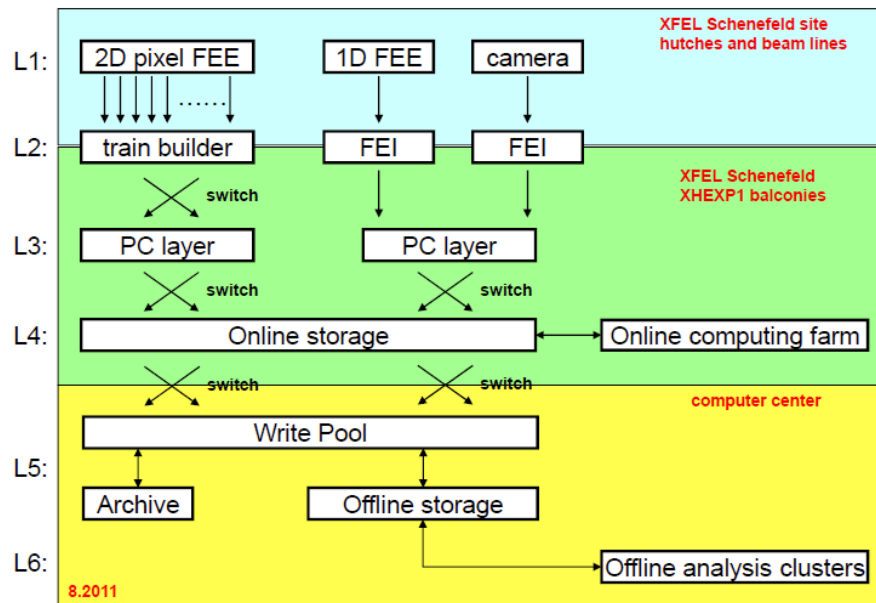
**Figure 24:** *The common XFEL.EU data handling architecture with six layers. Figure courtesy of C. Youngman.*

## Data acquisition

The baseline MID instrument principle detectors are likely to be a 4.5 MHz repetition rate 1 Mpx 2D camera and, possibly, a similar-size CCD camera for imaging with high spatial resolution and low energy applications.

The AGIPD detector design currently allows a maximum of ~ 300 frames per pulse train and a 1k x 1k detector will produce 600 MB/train. For comparison, a pnCCD or an Eiger detector could acquire about 1 or 12 frames, respectively, per train, which, assuming 1 Mpx detectors, produces data volumes between 2 and 24 MB/train. At 10Hz train rates the AGIPD, pnCCD and Eiger detectors produce 6 GB/s, 20 MB and 240 MB/s, respectively.

The readout architecture at XFEL foresees that the front-end electronics (FEE) modules of detectors connect to a front-end readout interface (FEI) which builds the detector data of each pulse acquired into a complete frame, and insert all frames recorded in a train (macro pulse) into a contiguous block for transfer to the PC layer, see Figure 24. The XFEL.EU FEI (train builder) is developed primarily for AGIPD type area detectors with very challenging data rates, but can also be used directly by commercial cameras provided that readout link and timing interface definitions are respected. Once acquired in the train builder the data is transferred to the backend PC layer. Auto-correlation experiments should in particular profit from the design of the

readout architecture which keeps all frames of a train together and respects the order.

## Data management

The MID instrument will be used for SAXS and WAXS experiments in XPCS and imaging modes. Taking into account sample handling, alignment, etc. acquisition is expected for a maximum of 50% of the beam time. Depending on the experimental details, the number of frames to be collected per run is $10^3$ to $10^6$. The extremely large data volumes generated by the detectors described above (~ 300 TB per day of raw data, assuming 50% utilization), and at XFEL in general, require a paradigm change in how data and analysis are managed; storage and bulk analysis of experiment data will primarily be performed onsite with local analysis clusters and not at users' home institutes. Consequently, centralized management services must be provided that allow this. These services include data catalogues, databases, file format implementations, user access authentication and authorization services, remote computing, etc. A software and hardware framework that technically implements the above features will be provided by XFEL.EU.

A key feature of the data processing is that poor quality data be rejected as early as possible. In layers where conventional computing power (CPU or GPU) is present, this is performed using the framework provided by the XFEL.EU, which allows experiment-specific software modules to be integrated and used to reject data. In this respect, quick feedback of quality-of-data parameters, e.g. contrast and correlation shape during auto-correlation measurements or quick reconstructions in diffraction imaging experiments, will be important and this should be foreseen. Additionally, a VETO system is being developed for use with FEEs that provides an additional rejection mechanism alleviating the limited storage pipeline lengths associated with the sensor ASICs of the 2D detectors. The pipeline slots for bad quality frames can be cleared for reuse by a timely arrival of a VETO signal at the FEE. In view of the large raw data volumes created, data volume reduction by compression, zero suppression, etc. will be have to be applied as early as possible in the data handling scheme.

Data rejection and reduction will therefore be possible either at the FEE, in the online mode on the PC layer, or just after the data is temporarily stored on

the DAQ data cache. The raw data from unsuccessful experiments or from the alignment phase should not be stored in the archive. The reduced, good-quality data will be transferred to the archive and to the highly accessible disk servers for further analysis on site in the offline mode where additional reduction is possible

## Scientific computing

The European XFEL will provide a user friendly and fully integrated scientific computing facility that will run on onsite hardware. A major element of the scientific computing solution is the development of a software framework and toolkit that will be used in all layers, from scientific computing and data storage to detector and beamline control. The framework is designed to be extremely flexible with the aim to easily integrate external applications, allowing users to incorporate their own analysis software should they wish to. The framework provides a complete suite of tools including configuration, message oriented middleware, database access, process pipelining, bindings to other languages, a scriptable application interface as well as a GUI system. The Scientific Computing system being developed by XFEL.EU will exploit this framework to expedite user analysis of data. The aim is to develop software that allows the computation of correlation functions as well as phase retrieval by iterative algorithms with boundary conditions entirely defined by the user.

# Price estimate and time line

A rough price estimate and timeline for construction can be given, based on the items identified in this report. However, large uncertainties must be accepted as several items represent new developments and the price is not well known. The construction time needed depends to a large extent on the human resources available for designing, drawing, engineering support, and manufacturing.

| | |
|---|---|
| UHV Monochromators incl. cryo-cooler and piping | ~ 0.9 M€ |
| Long detector arm | ~ 0.8 M€ |
| Diffractometer | ~ 0.8 M€ |
| AGIPD detector + electronics | (covered by detector group) |
| SAXS-WAXS sample chamber | ~ 0.2 M€ |
| Optical table and local laser and X-ray optics | ~ 0.3 M€ |
| UHV slit units and attenuators | ~ 0.5 M€ |
| Crystal delay line | ~ 0.6 M€ |
| CRLs and UHV transfocator mechanics | ~ 0.5 M€ |
| Diagnostics units | ~ 0.4 M€ |
| UHV components and pumps | ~ 0.3 M€ |
| Electronics and cables | ~ 0.1 M€ |
| Computing equipment | ~ 0.2 M€ |
| Shielding and lead hutches with infrastructure | ~ 1.0 M€ |
| Control hutch | ~ 0.1 M€ |
| Additional detector budget | ~ 1.0 M€ |

This amounts to an estimated total investment budget of about 7.7 M€ for the MID station. Items located upstream of those indicated in Figure 20 (e.g. the offset mirrors) have not been considered here as they surely belong to other work package budgets. An additional detector budget to address the case for an area detector with smaller pixels have been included in the list of MID items but might be transferred to the detector group budget. The AGIPD detector will be provided by the detector group. One or several of the monochromators requested could be covered by the budget of WP73 (X-Ray Optics and Beam Transport) but a budget is included here for the sake of completeness. The price for the required lead hutches and their infrastructure are at present not well known and hence they represent the largest uncertainty in the estimated budget.

A full time engineer position is required to support the development of the technical design as soon as possible. It is estimated that a full time technician is needed from about one year before installation begins. In total about 20 FTE positions are required until 2016 to complete the MID station.

The time line for construction depends critically on the availability of engineering support to progress toward a technical design report (MID TDR). It is believed realistic that the MID TDR could be ready by spring 2013. However, it is conceivable that well-specified items could be dealt with separately beforehand and purchasing/manufacturing started within 12 months. This could happen almost without the need for additional engineering support and concerns in particular the diffractometer, the long detector arm, and the CRL units where the MID team and colleagues at the European XFEL possess the necessary knowledge.

# References

[1]     European XFEL Technical Design Report.
        http://xfel.desy.de/tdr/tdr/

[2]     MID Workshop:
        http://www.xfel.eu/events/workshops/2009/mid_workshop_2009/

[3]     G. Grübel, A. Madsen, A. Robert: "X-Ray Photon Correlation Spectroscopy (XPCS)",
        Chapter 18 in *Soft-Matter Characterization*, Springer (2008).
        http://www.springerlink.com/content/978-1-4020-4465-
        6#section=231761&page=1&locus=0

[4]     H. N Chapman, K.A. Nugent: "Coherent lensless X-ray Imaging", Nature Photonics **4**,
        833 (2010).
        http://www.nature.com/nphoton/journal/v4/n12/full/nphoton.2010.240.html

[5]     XPCS report from MID workshop:
        http://www.xfel.eu/sites/site_xfel-
        gmbh/content/e63594/e63599/e81232/e64013/e92121/MID-
        XPCS_Report_230610_eng.pdf

[6]     E.A. Schneidmiller, M.V. Yurkov: "Photon beam properties at the European XFEL",
        XFEL.EU TR-2011-006 (2011).
        http://flash.desy.de/sites2009/site_vuvfel/content/e403/e1642/e71562/e71563/infoboxC
        ontent76495/TESLA-FEL-2010-06.pdf

[7]     G. Grübel, G.B. Stephenson, C. Gutt, H. Sinn, Th. Tschentscher, "XPCS at the
        European X-ray free electron laser facility", Nuclear Instr. Meth. A **262**, 357 (2007).
        http://www.sciencedirect.com/science/article/pii/S0168583X07011068

[8]     P. Wochner, C. Gutt, T. Autenrieth, T. Demmer, V. Bugaev, A. Diaz Ortiz, A. Duri,
        F. Zontone, G. Grübel, H. Dosch: "X-ray cross correlation analysis uncovers hidden
        local symmetries in disordered matter", Proc. Natl. Acad. Sci. **106**, 11511 (2009).
        http://www.pnas.org/content/106/28/11511.full

[9]     W. Götze: "The essentials of the mode-coupling theory for glassy dynamics",
        Condensed Matter Physics **1**, 873 (1998).
        http://www.icmp.lviv.ua/journal/zbirnyk.16/008/art08.pdf

[10]    P.G. Debenedetti, F.H. Stillinger: "Supercooled liquids and the glass transition",
        Nature **410**, 259 (2001).
        http://www.nature.com/nature/journal/v410/n6825/full/410259a0.html

[11]    T. Seydel, A. Madsen, M. Tolan, G. Grübel, W. Press: "Capillary waves in slow motion",
        Phys. Rev. B **63**, 073409 (2001).
        http://prb.aps.org/abstract/PRB/v63/i7/e073409

[12]    Y. Chushkin, C. Caronna, A. Madsen, "Low-frequency elastic behavior of a supercooled
        liquid", Europhys. Lett. **83**, 36001 (2008).
        http://iopscience.iop.org/0295-5075/83/3/36001/

[13]    A. Duri, T. Autenrieth, L.-M. Stadler, O. Leupold, Y. Chushkin, G. Grübel, C. Gutt:
        "Two dimensional heterogeneous dynamics at the surface of a colloidal suspension",
        Phys. Rev. Lett. **102**, 145701 (2009).
        http://prl.aps.org/abstract/PRL/v102/i14/e145701

[14]    S. Streit, C. Gutt, V. Chamard, A. Robert, M. Sprung, H. Sternemann, M. Tolan:
        "Two-dimensional dynamics of metal nanoparticles on the surface of thin polymer films
        studied with coherent X-rays", Phys. Rev. Lett. **98**, 047801 (2007).
        http://prl.aps.org/abstract/PRL/v98/i4/e047801

[15] M. Sikorski, C. Gutt, Y. Chushkin, M. Lippmann, H. Franz: "Dynamics at the liquid-vapor interface of a supercooled organic glassformer", Phys. Rev. Lett. **105**, 215701 (2010). http://prl.aps.org/abstract/PRL/v105/i21/e215701

[16] H. Kim, A. Rühm, L.B. Lurio, J.K. Basu, J. Lai, D. Lumma, S.G.J. Mochrie, S.K. Sinha: "Surface dynamics of polymer films", Phys. Rev. Lett. **90**, 068302 (2003). http://prl.aps.org/abstract/PRL/v90/i6/e068302

[17] Z. Jiang, H. Kim, X. Jiao, H. Lee, Y.-J. Lee, Y. Byun, S. Song, D. Eom, C. Li, M.H. Rafailovich, L. B. Lurio, S. K. Sinha: "Evidence for viscoelastic effects in surface capillary waves of molten polymer films", Phys. Rev. Lett. **98**, 227801 (2007). http://prl.aps.org/abstract/PRL/v98/i22/e227801

[18] C. Gutt, M. Sprung, R. Fendt, A. Madsen, S.K. Sinha, M. Tolan: "Partially wetting thin liquid films: structure and dynamics studied with coherent X-rays", Phys. Rev. Lett. **99**, 096104 (2007). http://prl.aps.org/abstract/PRL/v99/i9/e096104

[19] H. Dosch: *Critical phenomena at surfaces and interfaces* (Springer-Verlag, Berlin, 1992)

[20] G. Brown, P.A. Rikvold, M. Sutton, M. Grant: "Speckle from phase-ordering systems", Phys. Rev. E **56**, 6601 (1997). http://pre.aps.org/abstract/PRE/v56/i6/p6601_1

[21] A. Fluerasu, M. Sutton, E.M. Dufresne: "X-ray intensity fluctuation spectroscopy studies on phase ordering systems", Phys. Rev. Lett. **94**, 055501 (2005). http://prl.aps.org/abstract/PRL/v94/i5/e055501

[22] K. Ludwig, F. Livet, F. Bley, J.-P. Simon, R. Caudron, D. LeBolloc'h, A. Moussaid, "X-ray intensity fluctuation spectroscopy studies of ordering kinetics in a Cu-Pd alloy", Phys. Rev. B **72**, 144201 (2005). http://prb.aps.org/abstract/PRB/v72/i14/e144201

[23] B.M. Murphy, H. Requardt, J. Stettner, J. Serrano, M. Krisch, M. Müller, W. Press: "Phonon modes at the 2H-NbSe$_2$ surface observed by grazing incidence inelastic X-ray scattering", Phys. Rev. Lett. **95**, 256104 (2005). http://prl.aps.org/abstract/PRL/v95/i25/e256104

[24] A. Madsen, B.L. Leheny, H. Guo, M. Sprung, O. Czakkel: "Beyond simple exponential correlation functions and equilibrium dynamics in x-ray photon correlation spectroscopy", New. J. Phys. **12**, 055001 (2010). http://iopscience.iop.org/1367-2630/12/5/055001/pdf/1367-2630_12_5_055001.pdf

[25] C. Caronna, Y. Chushkin, A. Madsen, A. Cupane: "Dynamics of nanoparticles in a supercooled liquid", Phys. Rev. Lett. **100**, 055702 (2008). http://prl.aps.org/abstract/PRL/v100/i5/e055702

[26] H. Guo, G. Bourret, M.K. Corbierre, S. Rucareanu, R.B. Lennox, K. Laaziri, L. Piche, M. Sutton, J.L. Harden, R.L. Leheny: "Nanoparticle motion within glassy polymer melts", Phys. Rev. Lett. **102**, 075702 (2009). http://prl.aps.org/abstract/PRL/v102/i7/e075702

[27] D. Lumma, L.B. Lurio, S.G.J. Mochrie, M. Sutton: "Area detector based photon correlation in the regime of short data batches: Data reduction for dynamic x-ray scattering", Rev. Sci. Instrum. **71**, 3274 (2000). http://rsi.aip.org/resource/1/rsinak/v71/i9/p3274_s1

[28] R. Bandyopadhyay, D. Liang, H. Yardimci, D.A. Sessoms, M.A. Borthwick, S.G.J. Mochrie, J.L. Harden, R.L. Leheny: "Evolution or particle-scale dynamics in an aging clay suspension", Phys. Rev. Lett. **93**, 228302 (2004). http://prl.aps.org/abstract/PRL/v93/i22/e228302

[29] H. Guo, S. Ramakrishnan, J.L. Harden, R.L. Leheny: "Connecting nanoscale motion and rheology of gel-forming colloidal suspensions", Phys. Rev. E **81**, 050401 (2010). http://pre.aps.org/abstract/PRE/v81/i5/e050401

[30] O. Czakkel, A. Madsen: "Evolution of structure and dynamics during formation of a cross-linked polymer gel", Europhys. Lett. **95**, 28001 (2011).
http://iopscience.iop.org/0295-5075/95/2/28001

[31] W. Roseker, H. Franz, H. Schulte-Schrepping, A. Ehnes, O. Leupold, F. Zontone, S. Lee, A. Robert, G. Grübel: "Development of a hard X-ray delay line for X-ray photon correlation spectroscopy and jitter-free pump-probe experiments at X-ray free electron laser sources", J. Sync. Rad. **18**, 481 (2011).
http://scripts.iucr.org/cgi-bin/paper?S0909049511004511

[32] R. Bandyopadhyay, A.S. Gittings, S.S. Suh, P.K. Dixon, D.J. Durian: "Speckle-visibility spectroscopy: A tool to study time-varying dynamics", Rev. Sci. Instr. **76**, 093110 (2005).
http://ieeexplore.ieee.org/xpl/freeabs_all.jsp?arnumber=5001954

[33] D. L. Abernathy, G. Grübel, S. Brauer, I. McNulty, G.B. Stephenson, S.G.J. Mochrie, A.R. Sandy, N. Mulders, M. Sutton: "Small-angle scattering using coherent undulator radiation at the ESRF", J. Sync. Rad. **5**, 37 (1998).
http://journals.iucr.org/s/issues/1998/01/00/issconts.html

[34] E. Beaurepaire, J.C. Merle, A. Daunois, J. Y. Bigot: "Ultrafast spin dynamics in ferromagnetic nickel", Phys. Rev. Lett. **76**, 4250 (1996).
http://prl.aps.org/abstract/PRL/v76/i22/p4250_1

[35] S.T. Bramwell, M.J.P. Gingras: "Spin ice state in frustrated magnetic pyrochlore materials", Science **294**, 1495 (2001).
http://www.sciencemag.org/content/294/5546/1495.abstract

[36] J.M. Tranquada, B.J. Sternlieb, J.D. Axe, Y. Nakamura, S. Uchida: "Evidence for stripe correlations of spins and holes in copper oxide superconductors, Nature **375**, 561 (1995).
http://www.nature.com/nature/journal/v375/n6532/abs/375561a0.html

[37] I.A. Zaliznyak, J.P. Hill, J.M. Tranquada, R. Erwin, Y. Moritomo: "Independent freezing of charge and spin dynamics in $La_{1.5}Sr_{0.5}CoO_4$", Phys. Rev. Lett. **85**, 4353 (2000).
http://prl.aps.org/abstract/PRL/v85/i20/p4353_1

[38] Z. Kam, M.H. Koch, J. Bordas: "Fluctuation x-ray scattering from biological particles in frozen solution by using synchrotron radiation", Proc. Natl. Acad. Sci. USA **78**(6), 3559 (1981).
http://www.pnas.org/content/78/6/3559.abstract

[39] J.M. Rodenburg, A.C. Hurst, A.G. Cullis, B.R. Dobson, F. Pfeiffer, O. Bunk, C. David, K. Jefimovs, I. Johnson: "Hard-X-Ray Lensless Imaging of Extended Objects", Phys. Rev. Lett. **98**, 034801 (2007).
http://prl.aps.org/abstract/PRL/v98/i3/e034801

[40] M. Dierolf, A. Menzel, P. Thibault, P. Schneider, C. M. Kewish, R. Wepf, O. Bunk, F. Pfeiffer: "Ptychographic X-ray computed tomography at the nanoscale", Nature **467**, 436–439 (23 September 2010).
http://www.nature.com/nature/journal/v467/n7314/full/nature09419.html

[41] L.-M. Stadler, C. Gutt, T. Autenrieth, O. Leupold, S. Rehbein, Y. Chushkin, G. Grübel: "Hard X Ray Holographic Diffraction Imaging", Phys. Rev. Lett. **100**, 245503 (2008).
http://prl.aps.org/abstract/PRL/v100/i24/e245503

[42] V. Chamard, J. Stangl, G. Carbone, A. Diaz, G. Chen, C. Alfonso, C. Mocuta, T.H. Metzger: "Three-Dimensional X-Ray Fourier Transform Holography: The Bragg Case", Phys. Rev. Lett. **104**, 165501 (2010).
http://prl.aps.org/abstract/PRL/v104/i16/e165501

[43] X. Huang, J. Nelson, J. Kirz, E. Lima, S. Marchesini, H. Miao, A.M. Neiman, D. Shapiro, J. Steinbrener, A. Stewart, J.J. Turner, Chris Jacobsen, "Soft X-Ray Diffraction Microscopy of a Frozen Hydrated Yeast Cell", Phys. Rev. Lett. **103**, 198101 (2009).
http://prl.aps.org/abstract/PRL/v103/i19/e198101

[44] E. Lima, L. Wiegart, P. Pernot, M. Howells, J. Timmins, F. Zontone, A. Madsen: "Cryogenic X-Ray Diffraction Microscopy for Biological Samples", Phys. Rev. Lett. **103**, 198102 (2009).
http://prl.aps.org/abstract/PRL/v103/i19/e198102

[45] D. Shapiro, P. Thibault, T. Beetz, V. Elser, M. Howells, C. Jacobsen, J. Kirz, E. Lima, H. Miao, A. M. Neiman, D. Sayre: "Biological imaging by soft x-ray diffraction microscopy", Proc. Natl. Acad. Sci. USA **102**, 15343 (2005).
http://www.pnas.org/content/102/43/15343

[46] A.P. Mancuso et al.: "Coherent-Pulse 2D Crystallography Using a Free-Electron Laser X-Ray Source", Phys. Rev. Lett. **102**, 035502 (2009).
http://prl.aps.org/abstract/PRL/v102/i3/e035502

[47] M.H.J. Koch, N.A. Dencher, D. Oesterhelt, H.-J. Plöhn, G. Rapp, G. Büldt: "Time-resolved X-ray diffraction study of structural changes associated with the photocycle of bacteriorhodopsin", The EMBO Journal **10**, 521 (1991).
http://www.ncbi.nlm.nih.gov/pmc/articles/PMC452679/pdf/emboj00101-0024.pdf

[48] E.M. Landau, J.P. Rosenbusch: "Lipidic cubic phases – a novel concept for the crystallization of membrane proteins", Proc. Natl. Acad. Sci. USA **93**, 14532 (1996).
http://www.pnas.org/content/93/25/14532.full.pdf

[49] M. Tegze, G. Faigel: "X-ray holography with atomic resolution", Nature **380**, 49 (1996).
http://www.nature.com/nature/journal/v380/n6569/abs/380049a0.html

[50] S. Eisebitt, J. Lüning, W. F. Schlotter, M. Lörgen, O. Hellwig, W. Eberhardt, J. Stöhr: "Lensless imaging of magnetic nanostructures by X-ray spectro-holography", Nature **432**, 885 (2004).
http://www.nature.com/nature/journal/v432/n7019/abs/nature03139.html

[51] S. Marchesini et al.: "Massively parallel X-ray holography", Nature Photonics **2**, 560 (2008).
http://www.nature.com/nphoton/journal/v2/n9/abs/nphoton.2008.154.html

[52] G.J. Williams, M.A. Pfeifer, I.K. Vartanyants, I.K. Robinson: "Three-dimensional imaging of microstructure in gold nanocrystals". Phys. Rev. Lett. **90**, 175501 (2003).
http://prl.aps.org/abstract/PRL/v90/i17/e175501

[53] M.A. Pfeifer, G.J. Williams, I A. Vartanyants, R. Harder, R. & I.K. Robinson: "Three-dimensional mapping of a deformation field inside a nanocrystal", Nature **442**, 63 (2006).
http://www.nature.com/nature/journal/v442/n7098/full/nature04867.html

[54] J. Miao, C.-C. Chen, C. Song, Y. Nishino, Y. Kohmura, T. Ishikawa, D. Ramunno-Johnson, T.-K. Lee, S.H. Risbud: "Three-Dimensional GaN-Ga$_2$O$_3$ Core Shell Structure Revealed by X-Ray Diffraction Microscopy", Phys. Rev. Lett. **97**, 215503 (2006).
http://prl.aps.org/abstract/PRL/v97/i21/e215503

[55] M.C. Newton, S.J. Leake, R. Harder, I.K. Robinson: "Three-dimensional imaging of strain in a single ZnO nanorod", Nature Materials **9**, 120 (2009).
http://www.nature.com/nmat/journal/v9/n2/abs/nmat2607.html

[56] J. Gulden, O. M. Yefanov, A.P. Mancuso, V.V. Abramova, J. Hilhorst, D. Byelov, I. Snigireva, A. Snigirev, A.V. Petukhov, I.A. Vartanyants: "Coherent x-ray imaging of defects in colloidal crystals", Phys. Rev. B **81**, 224105 (2010).
http://prb.aps.org/abstract/PRB/v81/i22/e224105

[57] A.A. Minkevich, E. Fohtung, T. Slobodskyy, M. Riotte, D. Grigoriev, T. Metzger, A.C. Irvine, V. Novák, V. Holý, T. Baumbach: "Strain field in (Ga,Mn)As/GaAs periodic wires revealed by coherent X-ray diffraction", Europhys. Lett. **94**, 66001 (2011).
http://iopscience.iop.org/0295-5075/94/6/66001

[58] K.S. Raines, S. Salha, R.L. Sandberg, H. Jiang, J.A. Rodríguez, B.P. Fahimian, H.C. Kapteyn, J. Du, J. Miao: "Three-dimensional structure determination from a single

view", Nature **463**, 214 (2010).
http://www.nature.com/nature/journal/v463/n7278/full/nature08705.html

[59]  H.F. Poulsen: *Three-Dimensional X-ray Diffraction Microscopy. Mapping Polycrystals and their Dynamic*  (Springer, 2004)

[60]  A. Alpers, G.T. Herman, H.F. Poulsen, S. Schmidt: "Phase retrieval for superposed signals from multiple binary objects", J. Opt. Soc. Am. A **27**, 1927 (2010).
http://www.opticsinfobase.org/abstract.cfm?URI=josaa-27-9-1927

[61]  H. Tanaka, T. Kawasaki, H. Shintani, K. Watanabe: "Critical-like behavior of glass-forming liquids", Nature Materials **9**, 324 (2010).
http://www.nature.com/nmat/journal/v9/n4/abs/nmat2634.html

[62]  ID15's ESRF homepage:
http://www.esrf.eu/UsersAndScience/Experiments/StructMaterials/ID15

[63]  E. Jakeman in *Photon Correlation and Light Beating Spectroscopy*, edited by H. Z. Cummins and E. R. Pike, pp. 75-149 (Plenum, New York, 1973)

[64]  P.N. Pusey in *Photon Correlation Spectroscopy and Velocimetry*, edited by H. Z. Cummins and E. R. Pike, pp. 45-141 (Plenum, New York, 1977)

[65]  P. Falus, L.B. Lurio, S.G.J. Mochrie: "Optimizing the signal-to-noise ratio for X-ray photon correlation spectroscopy", J. Sync. Rad. 13, 253 (2006).
http://journals.iucr.org/s/issues/2006/03/00/bf5007/

[66]  Prof. Mark Sutton's XPCS coherence notes on the web:
http://www.physics.mcgill.ca/~mark/coherence/yorick/highqbeta.pdf

[67]  F. Livet, F. Bley, J. Mainville, R. Caudron, S.G.J. Mochrie, E. Geissler, G. Dolino, D. Abernathy, G. Grübel, M. Sutton: "Using direct illumination CCDs as high-resolution area detectors for X-ray scattering", Nucl. Instr. Meth. A **451**, 596 (2000).
http://www.sciencedirect.com/science/article/pii/S0168900200003338

[68]  J.W. Goodman, "Statistical properties of laser speckle patterns" in *Laser Speckle and Related Phenomena*, edited by J.C. Dainty (Springer, 1975)

[69]  X. Huang, J. Nelson, J. Steinbrener, J. Kirz, J.J. Turner, C. Jacobsen: "Incorrect support and missing center tolerances of phasing algorithms", Optics Express **18**, 26441 (2010).
http://www.opticsinfobase.org/abstract.cfm?uri=oe-18-25-26441

[70]  G. Geloni, V. Kocharyan, E. Saldin: "A simple method for controlling the line width of SASE X-ray FELs", DESY Report 10-053. arXiv:1004.4067v1 [physics.acc-ph]
http://arxiv.org/abs/1004.4067

[71]  H. Sinn et al.: "Conceptual Design Report: X-Ray Optics and Beam Transport", XFEL.EU TR-2011-002 (2011).
http://edmsdirect.desy.de/edmsdirect/file.jsp?edmsid=2081421

[72]  W. Decking, private communication

# Acknowledgements